A global screen for assembly state changes of the mitotic proteome by SEC-SWATH-MS

Moritz Heusel[1,5], Max Frank[1], Mario Köhler[2], Sabine Amon[1], Fabian Frommelt[1], George Rosenberger[1], Isabell Bludau[1], Simran Aulakh[1], Monika I. Linder[2], Yansheng Liu[3], Ben C. Collins[4], Matthias Gstaiger[1], Ulrike Kutay[2,*], Ruedi Aebersold[1,6,*]ℓ.

1 Institute of Molecular Systems Biology, Department of Biology, ETH Zurich, Zurich, Switzerland.

2 Institute of Biochemistry, Department of Biology, ETH Zurich, Zurich, Switzerland.

3 Department of Pharmacology, Yale University School of Medicine, New Haven, CT 06520, USA

4 School of Biological Sciences, Queen's University of Belfast, UK

5 Division of Infection Medicine (BMC), Department of Clinical Sciences, Lund University, Lund, Sweden

6 Faculty of Science, University of Zurich, Zurich, Switzerland.

ℓ Corresponding author & Lead contact

* Senior authors

Title

A global screen for assembly state changes of the mitotic proteome by SEC-SWATH-MS

Authors

Moritz Heusel[1,5], Max Frank[1], Mario Köhler[2], Sabine Amon[1], Fabian Frommelt[1], George Rosenberger[1], Isabell Bludau[1], Simran Aulakh[1], Monika I. Linder[2], Yansheng Liu[3], Ben C. Collins[4], Matthias Gstaiger[1], Ulrike Kutay[2*], Ruedi Aebersold[1,6*]]

Affiliations

1 Institute of Molecular Systems Biology, Department of Biology, ETH Zurich, Zurich, Switzerland.

2 Institute of Biochemistry, Department of Biology, ETH Zurich, Zurich, Switzerland.

3 Department of Pharmacology, Yale University School of Medicine, New Haven, CT 06520, USA

4 School of Biological Sciences, Queen's University of Belfast, UK

5 Division of Infection Medicine (BMC), Department of Clinical Sciences, Lund University, Lund, Sweden

6 Faculty of Science, University of Zurich, Zurich, Switzerland.

Author list footnotes

* Senior authors

] Corresponding author & Lead contact

Corresponding author(s) email address(es)

aebersold@imsb.biol.ethz.ch

Summary

Living systems integrate biochemical reactions that determine the functional state of each cell. Reactions are primarily mediated by proteins that have in systematic studies been treated as independent entities, disregarding their higher level organization into complexes which affects their activity and/or function and is thus of great interest for biological research. Here, we describe the implementation of an integrated technique to quantify cell state-specific changes in the physical arrangement of protein complexes, concurrently for thousands of proteins and hundreds of complexes. Applying this technique for comparison of human cells in interphase and mitosis, we provide a systematic overview of mitotic proteome reorganization. The results recall key hallmarks of mitotic complex remodeling and discover new events, such as a new model of nuclear pore complex disassembly, validated by orthogonal methods. To support the interpretation of quantitative SEC-SWATH-MS datasets, we extend the software *CCprofiler* and provide an interactive exploration tool, *SECexplorer-cc*.

Highlights

- Quantification of proteome assembly state changes using SEC-SWATH-MS
- Systems-wide analysis of assembly state changes in the mitotic proteome
- Discovery and validation of a novel mitotic disassembly intermediate of the nuclear pore complex
- Higher sensitivity and information content compared to thermostability-based approaches for global measurement of proteome states
- *SECexplorer*, an online platform to browse results and investigate proteins newly implicated in cell division

Introduction

Living systems are characterized by a large number of biochemical functions that are tightly interconnected and coordinated (Hartwell et al., 1999; Ideker et al., 2001). Classical biochemical analyses have led to the association of many biochemical functions with proteins and protein complexes. The function of proteins and protein complexes depends on a defined 3D structure of individual proteins, as well as the composition and specific steric arrangement of proteins into protein-protein complexes. Detailed studies on tetrameric hemoglobin have shown that changes in the composition, arrangement or structure of the complex changes its activity (Pauling 1949), a seminal finding that has since become one of the hallmarks of molecular biology. Whereas much of our biochemical understanding is based on in-depth studies of specific complexes, these are time consuming and more importantly, disregard interactions and coordination between different complexes.

Driven primarily by genomics, life science research has been transformed by high throughput, data-driven approaches. Proteomics is the embodiment of this approach for proteins. To date, most proteomic studies have been carried out by *bottom up proteomics*, where proteins are denatured and cleaved into peptides which are then analyzed by mass spectrometry. Whereas this technology has reached a high level of maturity, information about the structure, the composition and steric arrangement of components in a complex are lost. Therefore, for the most part, proteomics has treated proteins as unstructured biopolymers, disregarding structure and organization into complexes as an important layer of function and control.

Recently, several techniques have been proposed that attempt to extend the large scale analysis of proteins towards the detection of conformational changes between different states ((Becher et al., 2018; Dai et al., 2018; Leuenberger et al., 2017; Liu and Fitzgerald, 2016; Schopper et al., 2017; Tan et al., 2018), towards the organization of proteins into complexes (Heusel et al., 2019; Kristensen et al., 2012; Scott et al., 2017; Wan et al., 2015) and towards assigning protein subcellular localization (Dunkley et al., 2004; Foster et al., 2006). Conformational changes of proteins have been detected by using changes in physico-chemical properties including thermostability ((Becher et al., 2018; Dai et al., 2018; Tan et al., 2018)), stability towards denaturing conditions (Xu et al., 2014) or altered protease susceptibility (Leuenberger et al., 2017; Liu and Fitzgerald, 2016; Schopper et al., 2017) as proxy. Inference of complex composition and subcellular localization has been based on chromatographic fractionation, typically by size exclusion chromatography (SEC), of native complexes (Kristensen et al., 2012; Larance et al., 2016; Liu et al., 2008) and subcellular fractions (Dunkley et al., 2004; Foster et al., 2006; Itzhak et al., 2016), followed by the mass spectrometric analysis of the resulting fractions. Pioneering, comparative analyses of co-

79 fractionation patterns of native complexes have revealed extensive re-organization of the
80 modular proteome across metazoans (Wan et al., 2015) and following induction of apoptosis
81 (Scott et al., 2017). However, the co-fractionation approach has been beset by limited SEC
82 resolution, and limitations inherent in data dependent analysis (DDA) mass spectrometry, the
83 method almost universally used in co-fractionation studies. These include limited proteomic
84 depth and accuracy of quantification and stochastic peptide sampling (Aebersold and Mann,
85 2016). Collectively, these limitations resulted in the need for multidimensional separation to
86 assign proteins to specific complexes and, for the most part, unknown error levels of complex
87 assignments (Kristensen et al., 2012; Scott et al., 2017; Stacey et al., 2017; Wan et al., 2015).
88 Recently, we demonstrated increased selectivity and overall performance in co-fractionation-
89 based profiling of cellular complexes using a workflow that is based on single dimension
90 fractionation by high resolution size exclusion chromatography, quantitative measurement of
91 polypeptide elution profiles by SWATH mass spectrometry, an instance of data independent
92 acquisition (DIA)(Gillet et al., 2012, 2016) and the introduction of a complex-centric data
93 analysis strategy (Heusel, Bludau et al., 2019). We also described a software tool *CCprofiler*,
94 that implements a complex-centric strategy to infer protein complexes and uses a target-decoy
95 model to assign a probability to each complex (Heusel, Bludau et al., 2019).

96 Here, we apply SEC-SWATH-MS to detect rearrangements in the modular proteome in HeLa
97 CCL2 cells in two cell cycle states, the interphase and prometaphase. We developed a
98 quantification module for the *CCprofiler* that supports the differential, quantitative analysis of
99 thousands of proteins and their association with complexes. We benchmark the
100 reproducibility of the integrated wet lab/computational method and compare its performance
101 to state-of-the art thermostability-based methods (Becher et al., 2018; Dai et al., 2018). We
102 validate the method by showing that it recapitulates known complex remodeling events
103 between the different states tested. We discover and validate by orthogonal methods a new
104 model of nuclear pore complex disassembly, thus demonstrating the potential of the method
105 to discover new biology. To support additional exploration of the present dataset and future
106 differential SEC-SWATH-MS datasets we provide an online tool, *SECexplorer-cc*.

107 We expect that the parallel quantification of abundance and compositional changes of
108 hundreds of protein complexes will significantly advance our understanding of biochemical
109 mechanisms and processes.

110 # Results

111 ## Generation of a SEC-SWATH-MS dataset for the detection of changes in the
112 organization of the mitotic proteome

113 As basis for our study into mitotic changes in the organization of the proteome, we applied the
114 previously described SEC-SWATH-MS workflow, in conjunction with targeted analysis
115 (Heusel, Bludau et al., 2019) in triplicate to cells synchronized in either cell cycle state as
116 illustrated in **Figure 1A.** Mild cellular extracts containing native proteins and protein
117 complexes were fractionated by high resolution SEC and the proteins in each fraction were
118 digested and quantitatively profiled across the chromatographic fractions by SWATH mass
119 spectrometry (Collins et al., 2017; Gillet et al., 2012; Röst et al., 2014). The samples tested
120 were Hela CCL2 cells synchronized in interphase or mitosis. We inferred changes in complex
121 composition and quantity from the resulting protein apparent size distribution patterns. The
122 mitotic arrest of the respective synchronized cell populations was documented by microscopic
123 assessment of cell shape and the detection of mitosis-specific electrophoretic mobility shifts
124 of hyper-phosphorylated Nup53 and Histone H3 phosphorylation (**Supplemental Figure S1**
125 **A-C**). For each of the three replicates performed for either condition, 65 consecutive SEC
126 fractions were collected and for each fraction the proteins were digested and analyzed, by
127 SWATH-MS, generating a quantitative dataset consisting of a total of 390 SEC fractions. The
128 resulting dataset was computationally analyzed using the OpenSWATH software suite and a
129 project specific spectral library as prior information (see **Figure 2A** and experimental
130 procedures for details). Overall, the analysis identified 70,445 peptides associated with 5514
131 proteins at a TRIC target FDR of 5%. Upon SEC-informed filtering as described previously
132 (Heusel, Bludau et al., 2019), 60,891 peptides and 5,044 proteins were quantified with high
133 confidence across the chromatographic fractions and with an overall decoy-estimated protein
134 level false discovery rate of below 0.4% (see methods for details). Per mitotic condition, we
135 quantified 52,718 and 56,553 peptides resulting in 4,438 and 4,798 protein profiles in
136 interphase and mitosis, respectively (**Figure 1B**). The SEC conditions we used resolved
137 proteins and protein complexes ranging from ca. 5 MDa to 10 kDa with a peak capacity to
138 baseline-separate ca. 20 peaks and showed good reproducibility as apparent from UV/Vis
139 spectrometric traces from the respective samples (**Figure 1C**). The large absorbance at 280
140 nm observed in the low molecular weight range (fractions 63-80) originated from detergents
141 employed for mild lysis, as evidenced by the drop off of protein-level MS intensities beyond
142 fraction F55, in line with the 30 kDa molecular weight cutoff employed for sample workup
143 (**Figure 1D)**. Even though a comparably high resolution SEC method was used, we detected
144 in the range of ca. 1,200 to 2,000 proteins per fraction (**Figure 1D, lower panel**). Whereas
145 most proteins were detected in both conditions, 4,192 (83%) proteins appeared more readily

146 extractable from mitotic cells (**Figure 1B**). This is apparent from the lower cumulative ion
147 intensities across most fractions (**Figure 1D**) and is potentially a consequence of mitotic
148 reorganization including nuclear envelope breakdown. The thus generated set of protein
149 abundance profiles was the basis for the further analyses.

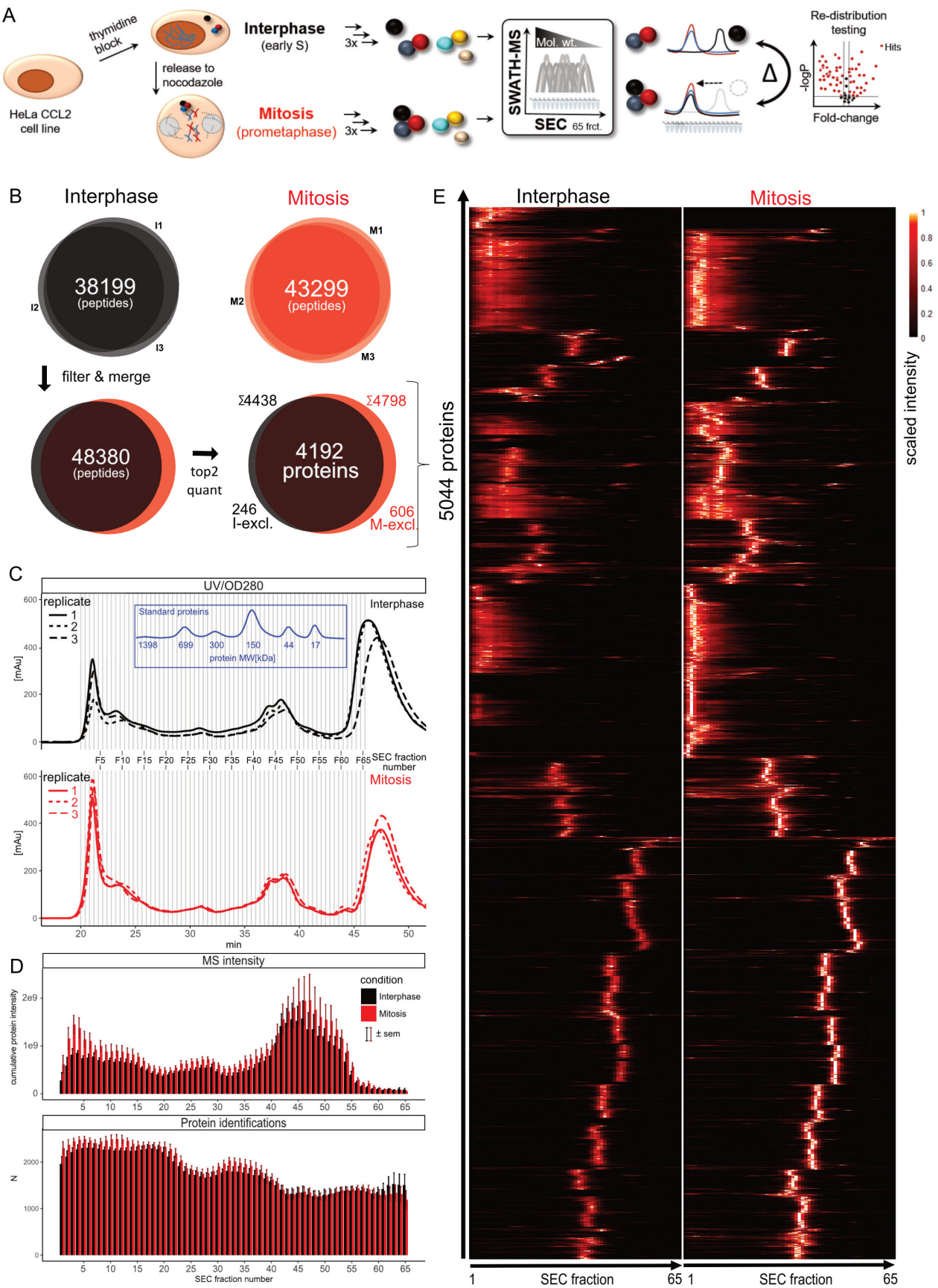

Figure 1: Proteome rearrangement screening by SEC-SWATH-MS: Workflow and dataset properties. **A** Scheme of the SEC-SWATH-MS workflow to screen for mitotic proteome rearrangement. HeLa CCL2 cells were

153 synchronized in interphase or mitosis by chemical treatment, followed by triplicate extraction of complexes by
154 mild lysis, fractionation by size exclusion chromatography and quantitative profiling of eluting proteins.
155 Differential association scoring via *CCprofiler* reveals proteins with altered complex association states between
156 conditions. **B** Peptide identifications across the three experimental repeats and summary per condition on peptide
157 and protein level, giving rise to the dataset overview in panel E. Of the total 5044 observed proteins, most were
158 detected independently in both conditions 4,192 (83%). **C** Semi-preparative scale SEC of interphasic and mitotic
159 complex preparations and size reference protein mix monitored by UV/Vis spectroscopy. Elution of standard
160 proteins calibrates the fraction number to apparent molecular weight mapping in the study. **D** Summary of MS-
161 observed protein level intensity and number of confidently identified proteins along the 65 fractions across the
162 repeats and after normalization (See data processing methods). The large absorbance at 280 nm observed in the
163 low molecular weight range originates from detergent employed for mild lysis and does not reflect protein mass
164 that was not sampled in the fractionation scheme, as can be extrapolated from protein-level MS intensities
165 dropping beyond F55, in line with the 30 kDa molecular weight cutoff employed in sample workup. **E** Dataset
166 overview heat map summarizing the data to 5,044 conditional protein elution patterns observed. Mean intensities
167 of the top 2 cumulatively highest-intense peptides per protein were summarized from 3 replicate measurements
168 and scaled from 0 to 1 per protein for visualization in heat map. Differential analysis is however performed at the
169 level of individual, protein-specific peptides (See **Figure 2**).

170 Quantification of protein association state changes from SEC-SWATH-MS data

171 The distribution of protein intensities per fraction for either condition provides a bird's eye
172 view of the acquired dataset (**Figure 1E).** To detect proteins that show significant changes
173 with respect to their association with specific protein complexes, we applied a scoring system
174 that quantifies protein mass re-distribution across distinct elution ranges based on two or more
175 proteotypic peptides quantified by SWATH-MS in each peak. The association of proteins
176 with protein complexes was carried out by the *CCprofiler* (Heusel, Bludau et al., 2019) a
177 software tool that implements a complex-centric strategy using prior knowledge of protein
178 complex composition. To detect quantitative changes of protein complex quantity and
179 composition in either cellular state, we added to the *CCprofiler* tool a new module supporting
180 differential quantification. It performs the sequential steps schematically shown in **Figure 2B**.

181 In the first step, signal intensities of SEC-fractions are normalized to a spike-in standard,
182 missing values are imputed using the background signals from neighboring SEC fractions and
183 SEC traces are aligned across experiments (**Figure 2B**, panel 1, for details and tools used see
184 experimental procedures). The result of the first step is a calibrated and refined list of peptides
185 and their respective intensities per fraction.

186 In the second step, the peptide level data are used to detect protein elution peaks along the
187 SEC dimension. This is achieved by selecting a high quality set of peptide traces, by summing
188 peptide intensities across replicates and conditions and by then employing the *CCprofiler*
189 protein-centric analysis module to infer protein elution peaks. An elution peak is derived from
190 the observation of co-eluting peaks of groups of sibling peptides derived from the same parent
191 protein (See **Figure 2B**, step 2. and peak detection summary and example in **Supplemental**
192 **Figure S4A&B**). This analysis resulted in a total of 6,040 elution peaks of 4,515 of the

193 identified proteins. Accordingly, protein-centric analysis successfully detects peptide co-
194 elution peak groups from 90% of the identified proteins and their peptide SEC profile sets,
195 with no high quality elution signal detectable for the remaining proteins at the confidence
196 threshold (q-value < 0.05). The distinctive elution peaks represent unique complex assembly
197 states of the respective proteins. Consistent with previous protein-centric analyses of the
198 proteome of cycling HEK293 cells (Heusel, Bludau et al., 2019), the majority of the observed
199 elution peaks in the present dataset fell into a SEC separation range consistent with the
200 association of the protein with a complex.

201 The distinctive protein elution peaks and their signal intensities computed in step two provide
202 the basis for the third step we term 'differential association testing'. Here, we calculated the
203 log2-transformed abundance of each peptide per replicate for each observed protein elution
204 peak in the six samples, resulting in six quantitative measurements per peptide per elution
205 peak. For each peptide, differential abundance was then tested for each elution event using a t-
206 statistic (**Figure 2B**, step 3. and exemplified for BAF53 in **Supplemental Figure S4B**). To
207 obtain a significance measure of differential abundance of individual protein elution peaks,
208 the median peptide level p-value of all peptides per protein per elution peak were integrated
209 based on a scoring scheme assuming a beta distribution of the respective values, as described
210 (Suomi and Elo, 2017). To generate the final differential protein association map, proteins are
211 represented by the peak with highest fold-change and shifting proteins assigned based on cut-
212 offs along the Benjamini-Hochberg-adjusted p-value (pBHadj score) and absolute SEC-
213 localized fold-change (**Figure 2B**, step 3, right panel).

214 In the last step, differential association to chromatographic peaks detected per protein is then
215 interpreted in the context of reference complexes to infer instances of protein complex
216 remodeling using the complex-centric concept (Heusel, Bludau et al., 2019) (**Figure 2B**, step
217 4 and exemplified in **Supplemental Figure S4C**). The results are finally visualized and
218 browsable via the web tool *SECexplorer-cc* as detailed further below. The extension of the
219 *CCprofiler* toolset by the quantification module thereby supports the automated detection of
220 altered protein association states and inferred protein complex remodeling from SEC-
221 SWATH-MS data and enables the detection of altered protein complexes that are at the core
222 of the present study.

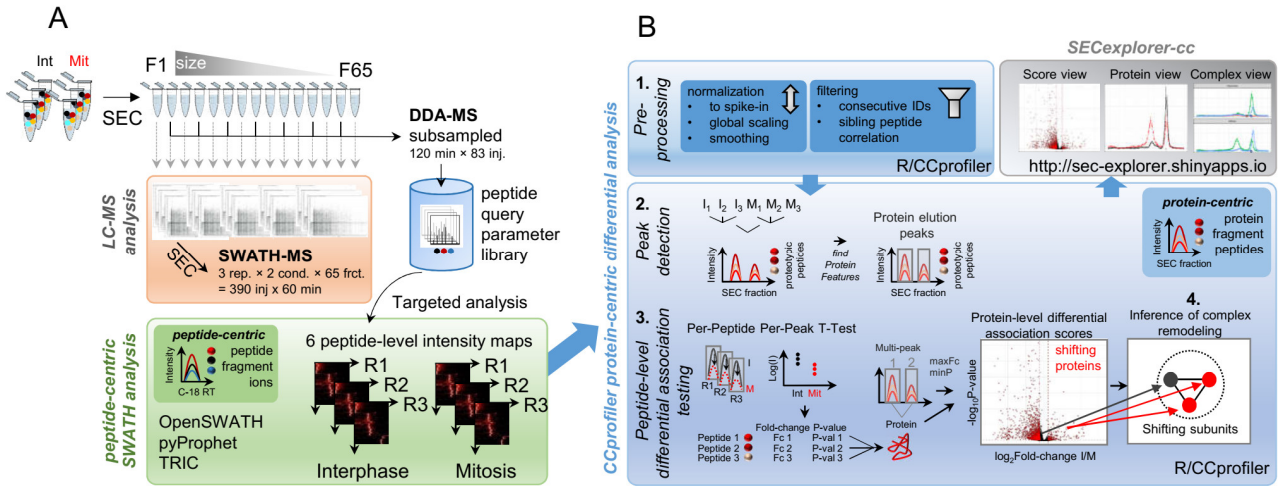

Figure 2: Proteome rearrangement screening by SEC-SWATH-MS: Data acquisition and processing. **A** LC-MS/MS analysis of tryptic peptides generated from 65 fractions per replicate and condition by data-independent acquisition SWATH mass spectrometry (SWATH-MS, n runs = 390). A subsampled set of fractions were subjected to longer 120 min gradient length analysis acquiring data in data-dependent mode to deepen coverage of the sample-specific peptide spectrum and query parameter libraries (DDA-MS, n = 83). Quantitative signals of the targeted peptides is then extracted from the SWATH-MS maps in peptide-centric analysis where peptide analytes are evidenced based on peptide fragment ion signal peak groups along C-18 chromatographic retention time. This produces six peptide-level quantitative matrices as basis for extracting information on protein complex association changes in subsequent differential analysis via *CCprofiler*. **B** Detailed scheme of protein-centric differential analysis of the quantitative peptide-level data via *CCprofiler* involving 1. preprocessing, 2. protein-centric elution peak detection where protein analytes are evidenced based on proteolytic peptide ('protein fragment') signal peak groups along SEC retention time/fraction number and 3. peak-resolved peptide-level statistical scoring to detect differentially associating proteins with shifting mass distribution across SEC fractions. In step 4, from the protein/subunit-level hits protein complex remodeling is inferred in a complex-centric fashion. The results are made available in easily browsable form via *SECexplorer-cc*.

Benchmarking the differential SEC-SWATH-MS workflow and software tool using the mitotic dataset

The application of the method described above to the triplicate data obtained from two cell cycle states indicated substantial rearrangement of the proteome. Specifically, 2,189 SEC elution peaks of 1,793 proteins showed significant changes in abundance (pBHadj score ≤ 0.01, absolute SEC-localized fold-change ≥ 1.5, **Figure 3A**) and 1,626 shifts in the SEC elution range of assembled higher-order complexes. In the following, we further assessed the results at three levels: First, the technical reproducibility of data generation and analysis, second, recall of rearrangements of complexes known to be altered between cell cycle states and third, comparison of the results with those obtained from an orthogonal method from samples in comparable cell cycle states. In particular, we compared the differential SEC-SWATH results with results obtained from the parallel measurement of protein

252 thermostability (Becher et al., 2018; Dai et al., 2018) from which changes in protein
253 complexes were inferred.

254 *Reproducibility*

255 The availability of three replicate SEC-SWATH-MS measurements of either cell cycle state
256 allowed us to assess the reproducibility of the method. Specifically, we evaluated technical
257 cross-replicate variability at the level of i) size exclusion chromatography by the UV/Vis
258 photospectrometric traces, ii) SWATH-MS by peptide and inferred protein identities and their
259 relative abundance and iii) the overall SEC-SWATH-MS workflow by the reproducibility of
260 protein-level SEC chromatograms. SEC fractionation was well-reproducible as is apparent
261 from the UV absorbance profiles ($\lambda = 280$ nm) shown in **Figure 1C**. Further, SWATH-MS
262 identified > 80% of detected peptides in all three replicates per cell cycle state and 48,380
263 peptides of 4,192 proteins in both cell cycle states. A total of 5,044 proteins were profiled
264 across both cell cycle states (**Figure 1B**). SWATH-MS quantified proteins with good
265 reproducibility as protein intensities were highly correlated across replicates and adjacent
266 fractions with an average Pearson's $R > 0.98$ between replicate fractions of the same
267 biological condition (**Supplemental Figure S2B**). The reproducibility of protein abundance
268 measurements was longitudinally affected by deteriorating mass spectrometer performance.
269 However, these progressive effects were efficiently compensated by normalization based on
270 reference spike-in peptides (**Supplemental Figure S2A** and see experimental procedures).
271 The high degree of reproducibility achieved for the overall workflow was further apparent
272 from protein-level SEC chromatograms reconstructed from the independent experimental
273 repeats (See replicate SEC chromatograms of a select set of proteins given in **Figure 3G** and
274 all protein-level chromatograms with error bars provided in **Supplemental Item 1** with
275 source data in **Supplemental Table 1**). Overall, these metrics demonstrate the level of
276 reproducibility of the SEC-SWATH-MS workflow towards the detection of differential
277 protein associations between the two cell cycle states.

278 *Recall of known biology of cell cycle states*

279 Mitotic processes have been extensively studied. We therefore related the results of this study
280 to known mechanisms of mitotic biology, first at the level of general patterns and second at
281 the level of specific complexes. First, we calculated the over representation in gene ontology
282 annotations of the 1793 proteins with shifts detected by SEC. In agreement with previous
283 knowledge the results indicate cell cycle state-dependent changes in the functional groups
284 "RNA splicing and mRNA binding events" (Dominguez et al., 2016), "cellular
285 reorganization" (Gong et al., 2007) and "ribonucleoprotein and macromolecular complexes"
286 (Linder et al., 2017) (**Figure 3B**). Second, we related the results obtained in this study to

287 specific complexes that are known to be present at different assembly states in the cell cycle
288 states tested (Vermeulen et al., 2003). The best confirmed and generally accepted events of
289 this type include the mitotic activation of CDK1 by binding to its partner cyclin B1 (Gavet
290 and Pines, 2010) and the mitotic disassembly of nuclear pore complexes (NPCs) (Linder et
291 al., 2017). We found both events confirmed by the SEC-SWATH data. **Figure 3C** shows the
292 rewiring of the CDK1 - cyclin B1 (CCNB1) module, supported by high differential
293 association testing scores. Specifically, the size-calibrated subunit elution profiles closely
294 reflected the formation of CDK1-CCNB1 complexes in the cell cycle state and indicated that
295 CDK1 subunits of the CDK1-CCNB1 complex were recruited from the monomer pool,
296 whereas the overall expression level of CDK1 across cell cycle states remained stable (**Figure**
297 **3D**). In contrast, CCNB1 subunits showed increased expression in mitosis (**Figure 3D**,
298 insert), consistent with current models of CDK1 regulation by periodic expression of CCNB1
299 (Vermeulen et al., 2003). Notably, only part of mitotic CDK1 transitioned to the complex-
300 assembled form, with 69% detected in the assembled and 31% of the total MS signal detected
301 in the monomeric range. Further, the dataset confirmed the mitotic disassembly of NPCs
302 (**Figure 3E&F**) with 26 of the 27 observed canonical subunits detected as SEC-shifting (out
303 of 32 bona fide components as defined by (Hoelz et al., 2016)). Nucleoporin SEC profiles
304 suggested protein mass re-distribution from a high molecular weight (MW) population of
305 higher order nucleoporin complexes (fraction 5, void volume peak with apparent MW ≥ 5
306 MDa) to lower MW signals representative of NPC sub-complexes. This is exemplified by the
307 SEC elution profiles of the inner ring complex members NUP188, NUP205 and NUP93 that
308 are known to be part of mitotic sub-complexes of the NPC (Linder et al., 2017) (**Figure 3E**).
309 Sub-complexes eluted in earlier fractions of elevated molecular weight compared to the
310 respective monomers (**Figure 3F,** note monomer expected fraction markers). The observed
311 profiles were highly reproducible across the experimental repeats (**Figure 3G**).

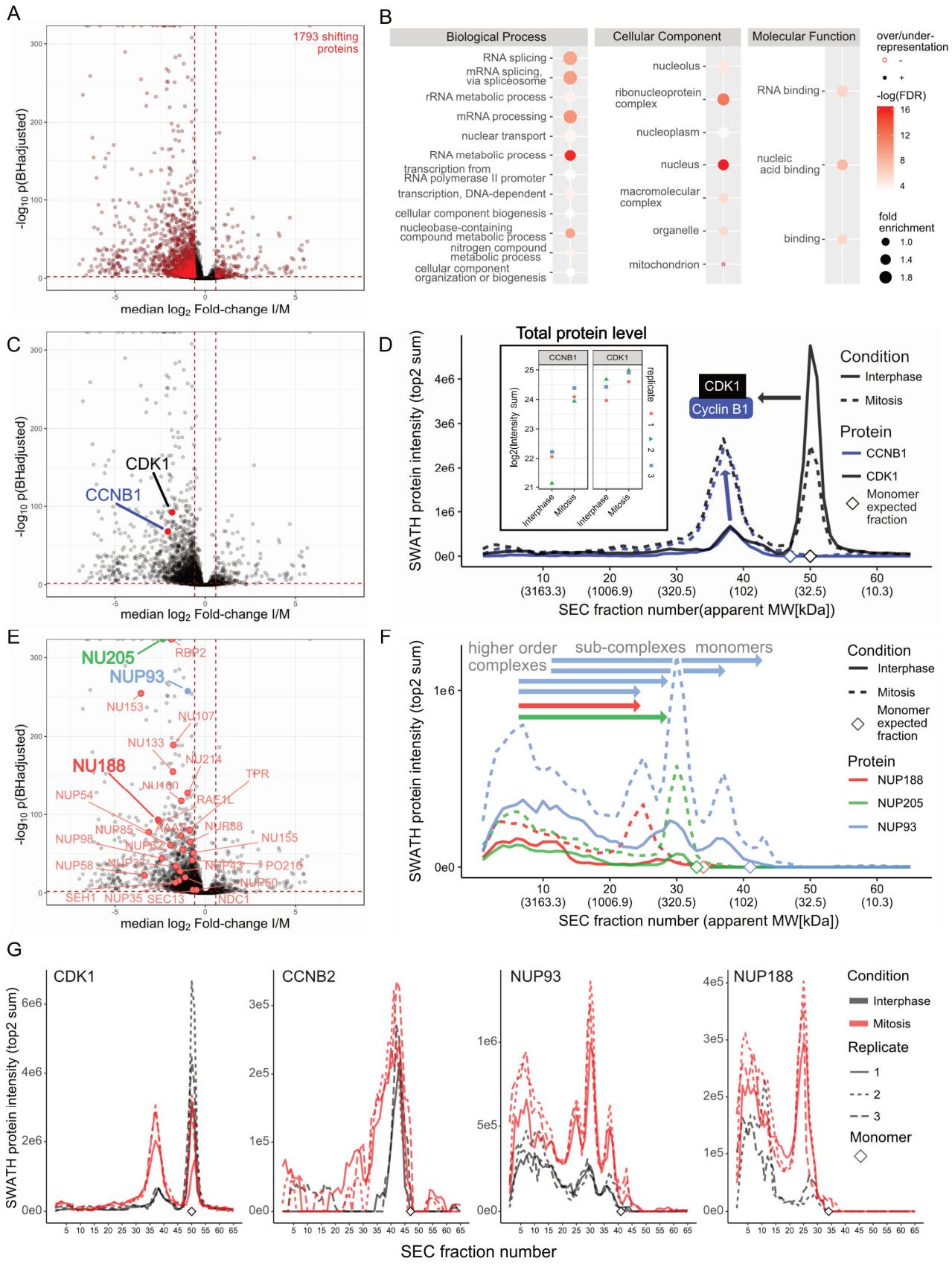

Figure 3: Benchmarking part 1: Recall of expected mitotic complex remodeling events. **A** Protein-level differential association score map highlighting 1,784 proteins shifting quantitative distribution across apparent sized assessed via SEC-SWATH. Benjamini-Hochberg adjusted P-value cutoff, ≤ 0.01; absolute SEC-localized fold-change ≥ 1.5 -fold. Reproducibility of SEC peptide and protein identification and quantification is assessed

317 in **Figure 1B-D**, protein level error chromatograms (**Supplemental item 1**) and protein intensity correlation
318 (**Supplemental Figure 2A**). **B** Gene ontology analysis of the total set of shifting proteins (PANTHERdb, against
319 the background of all 5,044 proteins detected) suggests activity in processes related to cell cycle progression. **C**
320 Protein-level differential association scores for a 'true positive' detection of an instance of mitotic complex
321 remodeling among cell cycle regulators cyclin-dependent kinase 1 (CDK1) and cyclin B1 (CCNB1). **D**
322 Conditional protein-level SEC chromatograms for CDK1 and CCNB1 capture and quantitatively characterize
323 mitosis-specific recruitment of 69 % of the CDK1-derived MS-signal (right panel) to the CCNB1-assembled
324 state. Inset: As expected, stable levels of CDK1 are observed while CCNB1 appears induced in mitosis (Total
325 intensity observed across the 65 SEC fractions). Diamonds mark the SEC fraction expected for respective
326 monomers based on naked sequence average molecular weight and external size calibration based on reference
327 protein fractionation (compare **Figure 1C**). **E** Protein-level differential association scores for a second instance
328 of 'true positive' detection of mitotic complex remodeling, nuclear pore complex disassembly. 26 of the 27
329 detectable subunits (out of 32 total, for assignment see experimental procedures) are detected to significantly
330 shift their SEC elution patterns (as assigned in panel **A** and see main text and methods). **F** Conditional protein-
331 level SEC chromatograms for an exemplary subset of protein components of the nuclear pore complex
332 disassembling upon mitotic entry. Protein-centric differential association scores are highlighted in panel **E**.
333 Chromatographic profiles of NUP188, NUP205 and NUP93 reveal protein mass re-distribution from high
334 molecular weight NPC complexes (fraction 5, apparent MW ≥ 5 MDa) to lower MW signals representative of
335 smaller NPC sub-complexes or likely a monomeric pool in the case of NUP93. Diamonds mark fractions where
336 monomer elution would be anticipated.

337 *Validation via orthogonal method.*

338 A significant strength of the present method is its ability to quantify changes in protein
339 complex abundance and chromatographic retention in a highly multiplexed manner. Recently,
340 orthogonal methods have been described that assess thermal stability variation. In these
341 methods changes in protein thermostability are used as a proxy for changes in protein
342 interaction and activity. This notion is supported by the observation of strikingly similar
343 thermostability profiles among subunits of the same complex (Tan et al., 2018). Two such
344 studies explored altered thermostability across the cell cycle (Becher et al., 2018; Dai et al.,
345 2018). They used chemical synchronization in early S and prometaphase, thus matching the
346 biological conditions analyzed in the present study. We therefore compared the results
347 obtained by the two orthogonal methods, SEC-SWATH-MS and thermal profiling,
348 represented by two instances of the approach termed Cellular Thermal Shift Assay (CETSA)
349 (Dai et al 2018) and Thermal Protein Profiling (TPP) (Becher et al, 2018).

350 First, we compared the proteome coverage achieved by the respective methods. The SEC-
351 SWATH-MS dataset identified 5,044 proteins. Of these 4,515 showed detectable SEC elution
352 peak(s) of which after statistical filtering 4,480 protein elution profiles were scored (for
353 details on dropouts see experimental procedures). This number is comparable to that achieved
354 by TPP (n = 4,780). CETSA achieved a markedly lower coverage at n = 2,773 proteins. More
355 than 600 proteins were exclusively characterized by SEC-SWATH-MS (**Figure 4A**).

356 Second, for each method we selected the 1000 proteins that showed highest scores indicating
357 mitotic change and compared the observability of expected patterns of mitotic change within
358 this set. For SEC-SWATH-MS the scoring was based on pBHadj/FC rank sum; for CETSA
359 on deltaFC and for TPP on local FDR and global FDR rank sum (**Figure 4B** and methods
360 section). For TPP, the selection of proteins along the combined rank sum included the
361 majority of the proteins reported as hits in the original study (**Supplemental Figure S4C**).
362 Unexpectedly, our analysis did not indicate higher similarity between the results of the two
363 thermostability based studies than between either of these studies and the SEC-SWATH-MS
364 derived data (274 proteins, 15.9%, shared between CETSA and TPP vs. 262 proteins, 15.1%,
365 shared between CETSA and SEC-SWATH-MS and 278 proteins, 16.1 %, shared between
366 TPP and SEC-SWATH-MS, **Figure 4C).** Whereas the three sets of top ranked proteins
367 showed a small overlap of 108 of 2,294 proteins, the functional and pathway enrichment
368 patterns of the three protein sets were in good agreement. All workflows uncovered strongest
369 activity changes in RNA processing and splicing processes and corresponding ribonuclear
370 complexes and the RNA binding machinery (**Figure 4D**).

371 The differential SEC-SWATH-MS analysis preferentially retrieves proteins in the GO
372 categories "nuclear transport", "proteins forming complexes" and "proteins of the nuclear
373 envelope" including components of the nuclear pore, while TPP exclusively retrieved proteins
374 associated with the ribosomal machinery. Both, SEC-SWATH-MS and CETSA detected
375 proteins associated with chromosome segregation, whereas this activity was not detected by
376 TPP. Membrane proteins appear underrepresented among the hits reported by SEC-SWATH-
377 MS and CETSA, but not TPP. Similarly, metabolic and enzymatic functions appear slightly
378 underrepresented in hits from SEC-SWATH-MS and TPP, but not CETSA (**Figure 4D**).

379 SEC-SWATH-MS exclusively showed a tendency to uncover proteins known to engage in
380 binding activities (**Figure 4D**, Molecular Function). Pathway enrichment analysis showed a
381 higher number of similar enrichments between SEC-SWATH-MS and CETSA and a more
382 strongly diverging pattern for the TPP results (**Supplemental Figure S3A**). To control for
383 biases introduced by our rank-based selection of the 1000 most regulated proteins from the
384 TPP results, we also included the hit list reported in the original study (897 Uniprot proteins
385 mapping unambiguously to the 923 reported hit gene names (Becher et al., 2018), Table S2,
386 see **Supplemental Figure S3B** for a comparison of the selected protein sets). Specifically,
387 SEC-SWATH-MS and CETSA both showed significant enrichment of pathway terms "Cell
388 Cycle / Mitotic Cell Cycle" and only SEC-SWATH-MS captured altered functional states of
389 the core cell-cycle regulator anaphase promoting complex APC/C and activation of the
390 mitotic spindle assembly checkpoint SAC (**Supplemental Figure S3A**). To explore potential
391 differences in the protein activities inferred from the protein properties measured by the

392 different methods (stability or size), we analyzed the biological process annotation of protein
393 sets reported exclusively by SEC-SWATH-MS (n = 568) and by both stability-based
394 approaches (n = 166) (**Supplemental Figure S3C**), respectively. Interestingly, the different
395 protein sets converge at the level of core regulated processes (RNA splicing & -processing)
396 and highly related processes. For instance, both protein sets point towards the assembly of
397 protein complexes, whereas changes in thermal stability were observed preferably in proteins
398 of ribosome and ribonucleoprotein complex biogenesis and changes in assembly state and size
399 were observed in proteins involved in protein-containing complex subunit assembly and -
400 organization. The measurement of both, thermal stability and size indicated alterations in
401 proteins from different metabolic processes, of which alterations in the category "organic
402 substance metabolic processes" were detected by either method. This may suggest that
403 alterations in metabolic processes can manifest in either protein stability or the assembly state
404 of complexes or both properties.

405 Third, we evaluated the recovery of proteins with known function in the cell-cycle process in
406 the respective datasets (UniProt functional annotation parsed on 'cell cycle', **Figure 4E**). The
407 SEC-SWATH-MS data showed the highest sensitivity for the measurement of altered protein
408 (association) states among the compared methods (**Figure 4E**, comparing sets from Venn
409 diagram in **Figure 4C**).

410 Fourth, we compared the sensitivity of the methods to recapitulate known biochemical events
411 of mitotic disassembly of NPCs. In this comparison, SEC-SWATH-MS showed the highest
412 degree of sensitivity as nucleoporins were ranked highest in the priority lists compared to the
413 priority lists generated by the other methods (**Figure 4F)**. This comparison validates the SEC-
414 SWATH-MS differential workflow to generate biological insights similar to those obtainable
415 via CETSA and at extended proteome coverage comparable to that achieved in the TPP
416 workflow.

417 Overall, these three levels of benchmarking showed high performance of the SEC-SWATH-
418 MS differential workflow, including the extended *CCprofiler* tool, to reveal altered protein
419 association states in biological samples with high sensitivity and broad proteomic coverage. In
420 addition, the chromatographic profiles contain extended layers of information such as the
421 specific composition and abundance of distinct complexes and also indicate quantitative
422 changes in protein abundance.

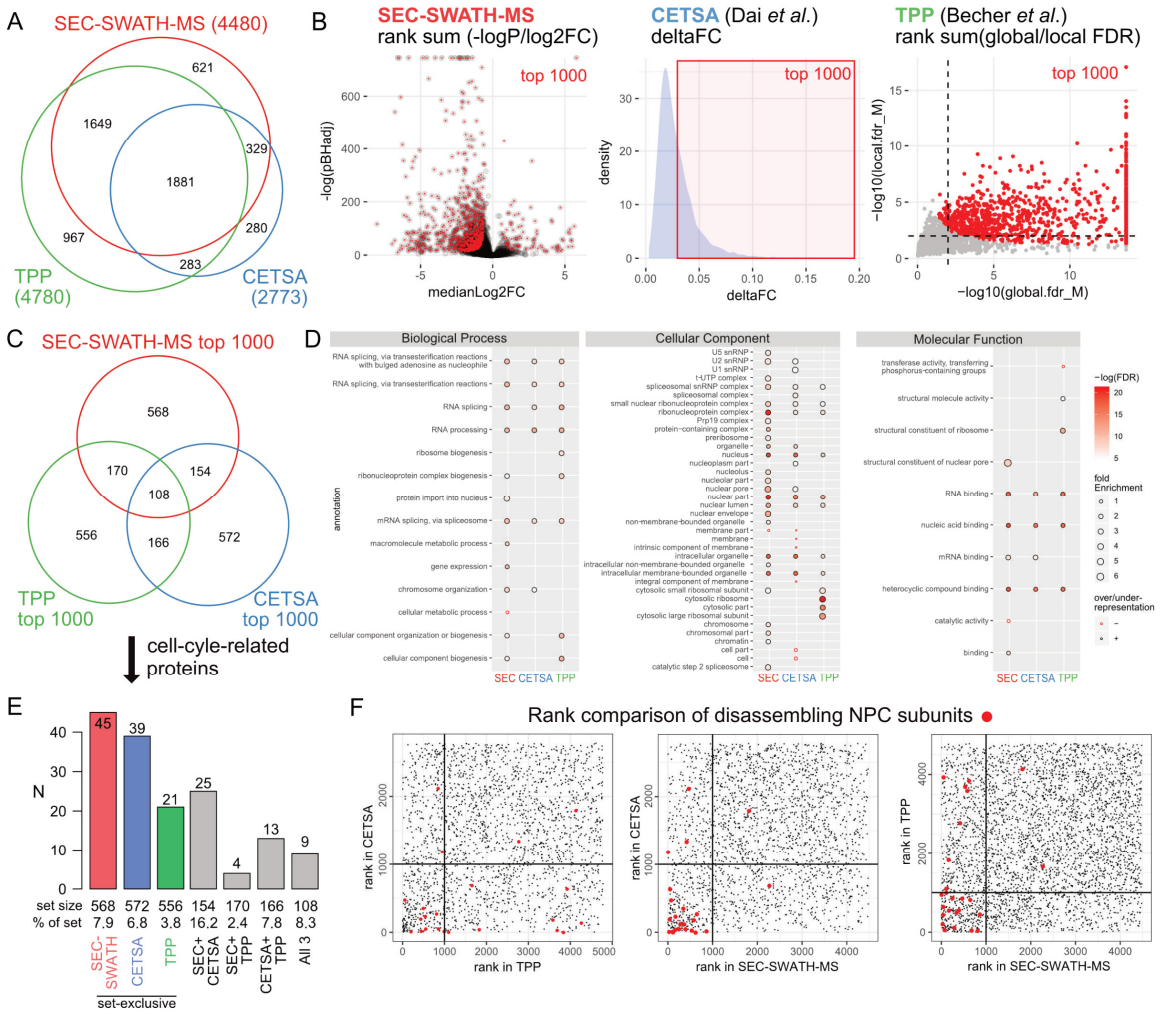

Figure 4: Benchmarking part 2: Performance of measuring proteome state dynamics by apparent size vs. thermostability. **A** Comparison of the total set of proteins characterized in SEC-SWATH (n = 4,480, this study), CETSA (Dai et al., 2018) (n = 2,773) and TPP (Becher et al., 2018) (n = 4,780). **B** Classification of top 1000 proteins to compare method performance. Proteins were ranked according to method-specific scores that intend to capture alterations in proteome association or thermostability state changes between cell populations chemically synchronized in distinct cell cycle stages (Comparison: interphase and prometaphase). All protocols employ thymidine block and nocodazole release experimental regimes. In SEC-SWATH-MS, top 1000 proteins are classified by linear combination of score ranks of equally weighted $\log_{10}$(pBHadj) and median $\log_2$ fold-change and selection along rank sum. Protein thermostability workflows employ two different scores (CETSA: delta fold-change; TPP: local and global FDR). The scores of the top 1000 proteins selected per method are indicated. To obtain protein ranks from the two scores in the TPP dataset, we combined the ranks along local and global FDR to select proteins along the rank sum. This procedure is equivalent to the protein ranking and selection procedure used for the SEC-SWATH-MS results. Dashed lines indicate the FDR cut-offs employed by the authors of the original study to select the 923 hits reported (Becher et al., 2018). **C** Comparison of top 1000 association- or stability-changing proteins detected in either approach shows degree of orthogonality and unexpectedly high dissimilarity of the protein sets reported to alter thermostability. **D** Gene ontology annotation overrepresentation testing of the top 1000 proteins per result set obtained from the three methods. Pathway enrichment is given in **Supplemental Figure S3**. **E** Comparison of method sensitivity based on method-exclusive recovery of 'true positive' proteins which function in relation to the cell cycle. Protein sets from Venn diagram in **C**. Cell-cycle-related proteins were defined by Uniprot annotation column 'Function' parsed on 'cell cycle'. Of these 289 proteins, 156 were covered by one or multiple of the compared methods. Recovered

445 numbers and rates with respect to set size suggest highest sensitivity of SEC-SWATH-MS and CETSA with
446 broader proteome coverage of SEC-SWATH-MS (4,480 vs 2,773 proteins in SEC-SWATH-MS vs. CETSA). **F**
447 Comparison of ranks of rearranging NPC component proteins in the three methods. Lowest rank means strongest
448 signal in the respective method. SEC-SWATH-MS ranks truly re-arranging proteins highest.

449 Inference of cell-cycle dependent complex remodeling

450 We used the quantitative, complex-centric SEC-SWATH-MS technique to detect changes in
451 complex quantity and composition between cell cycle states. These analyses are based on the
452 SEC profiles of 4,515 proteins forming 6,040 distinct peaks (*CCprofiler* protein-centric q-
453 value = 5%, see methods for details) and constitute a global 'master map' set of observable
454 protein features across replicates and conditions (See **Figure 2B** and **Supplemental Figure**
455 **S4A-B**). The chromatographic elution profile of each protein in the master map was analyzed
456 with respect to the following dimensions of information. First, the number of peaks in the
457 chromatographic range covering complex associated proteins indicated a minimal number of
458 distinct complexes a protein was associated with. Second, changes in chromatographic elution
459 between conditions identified proteins with significant changes of complex association, and
460 third, the correlation of peaks in the elution patterns of different proteins confirmed the
461 presence of specific complexes by complex-centric analysis. The data indicated that proteins
462 observed in two or more distinct complex-assembled states were enriched in signaling factors,
463 proteins with known binding functions and proteins involved in modulating post-translational
464 modification such as acetylation and phosphorylation (**Supplemental Figure S4D**). The data
465 further indicated that in most cases in which a protein was associated with different
466 complexes the SWATH-MS signals for independent peptides strongly correlated between
467 peaks, indicating overall very robust signal quality. Outlier peptides, i.e. peptides for which
468 the between-peak correlation deviated from the correlation of other peptides, likely indicate
469 cases of post-translational modifications resulting in the differential association of
470 proteoforms to different complexes.

471 The ensemble of protein SEC elution profiles further provided a base to estimate the fraction
472 of the proteome detected in monomeric or assembled form in either state. We designated
473 proteins as detected in an assembled state if their apparent MW based on the SEC elution was
474 minimally twofold larger than the predicted MW of the protein in monomeric form. The
475 protein SEC elution profiles were interrogated from two perspectives. First, we performed a
476 naïve assignment of protein intensity to either complex-assembled or monomeric state. To
477 make these assignments, we used the MS signals of the two most-abundant proteotypic
478 peptides per protein. In line with previous observations of the HEK293 proteome assembly
479 state via SEC-SWATH-MS (Heusel, Bludau et al., 2019), the major fraction of the interphasic
480 and mitotic HeLa CCL2 proteome mass was observed in complex-assembled state (57 ± 6%
481 and 58 ± 4%, respectively). In terms of protein numbers 70 ± 2% and 72 ± 2% of the proteins

482 were detected at least in part in complex assembled state in interphase and mitosis,
483 respectively.

484 To next explore differences in protein profiles observed between conditions, we applied
485 protein-centric peak detection per each cell cycle state. To increase signal-to-noise we merged
486 the three replicates and detected 5,291 and 5,637 distinct elution peaks for 4,083 and 4,264
487 proteins in interphase and mitosis, respectively. Based on the apex SEC fraction and
488 associated apparent molecular weight, the 1-5 elution peaks observed per protein were
489 assigned to likely assembled or monomeric pools of the total protein population (**Figure 5A**).
490 According to these assignments, 29 and 25% of proteins were observed eluting exclusively in
491 monomeric form, while 71 and 75% of proteins were observed in at least one complex-
492 assembled form in interphase and mitosis, respectively. A significant fraction of proteins was
493 further observed eluting in both, monomeric and complex assembled form(s) (12% in both
494 interphase and mitosis, respectively). These results indicate that in either cell cycle state a
495 significant fraction of the proteome was associated with complexes that are accessible to
496 differential quantification of protein association state changes via SEC-SWATH-MS and
497 *CCprofiler*.

498 We further used the ensemble of protein patterns to determine which proteins and associated
499 functions displayed a change in protein complex association between the two cell cycle states
500 tested. The data indicated substantial rearrangement of the proteome. Specifically, 2,189 SEC
501 elution peaks of 1,793 proteins showed significant abundance shifts. Of these, 1,626 shifts
502 were in the SEC elution range of complex-assembled proteins suggesting significant
503 rearrangements in the underlying complex(es) (**Figure 3A**, pBHadj score ≤ 0.01, absolute
504 SEC-localized fold-change ≥ 1.5). Proteins with altered complex association states were
505 predominantly associated with functions in "transcriptional and splice regulatory machinery"
506 and "cellular component organization" (**Figure 3B)**. The 1000 top-ranking proteins selected
507 for comparative benchmarking analyses further revealed reorganization in the MAPK cascade
508 (**Figure 4D**, Biological Process) and rearrangements involving central cell-cycle-associated
509 modules such as the APC/C, NPC and mitotic spindle checkpoint and mitotic anaphase
510 pathways, among others (**Figure S3A**).

511 Whereas these enrichment analyses already pointed at specific complexes undergoing mitotic
512 change, we next evaluated our results using the CORUM reference set of complexes as prior
513 information (Ruepp et al., 2010). Initially, we evaluated the rearrangements detected by SEC-
514 SWATH-MS that occur preferentially among protein complexes with known involvement in
515 mitotic processes. Indeed, we detected a higher frequency of changed patterns of proteins that
516 are known to associate into complexes, compared to a control group not known to be

517 affiliated with a complex (**Figure 5B**). On the level of individual proteins, the SEC-SWATH-
518 MS dataset covered over half of the subunits of the reference CORUM complexes (1473 of
519 2937). Of these, 702 showed significant changes in protein complex association between
520 states (**Figure 5C**, upper panel). More than half of the reference complexes were detected
521 based on two or more subunit proteins in our analysis (n = 949, **Figure 5C**, lower panel and
522 **Figure 5D**). Overall, 432 complexes showed evidence of remodeling based on significant
523 SEC shifts observed for minimally two of their subunits (**Figure 5E**). Among these changing
524 complexes, we observed preferential and more complete detection of changes in complexes
525 with known involvement in the cell cycle (**Figure 5F**). While many of the complexes with
526 evidence of remodeling are associated with known functions in relation to the cell cycle, a
527 significant fraction is not and thus present opportunities for further exploration. The
528 remodeled complexes and their functional annotation are summarized in **Supplemental Table**
529 **2**.

530 The results in **Figure 5G&H** illustrate two complexes without GO annotation for "cell cycle"
531 but with strong evidence for mitotic changes. For both complexes all CORUM subunits were
532 detected. The first is the cell-cycle-dependent assembly of the TRF2-RAP1 complex in
533 mitosis observed by strong SEC shift scores of both subunits and co-elution of RAP1 and
534 TRF2 with apex in SEC fraction 21 (ca. 950 kDa) in mitotic cells but not interphasic cells.
535 TRF2 was detected only in mitotic cells. In interphasic cells, RAP1 and showed no peak in
536 the SEC fraction range of the TRF2-RAP1 complex (**Figure 5G**). The results are in line with
537 the previously reported recruitment of RAP1 to telomeres via TRF2 and consistent with the
538 co-elution of the two proteins in the void volume (fractions 1-5, analytes >10 MDa) (**Figure**
539 **5G**, right panels). However, RAP1 was detected in the void volume of interphasic cells but
540 without the concurrent detection of TRF2. Notably, we did not observe the TRF2 and RAP1-
541 containing shelterin complex known to occupy telomeres in interphase (Liu et al., 2004),
542 likely due to low abundance and/or low recovery in mild lysis of interphase cells. In either
543 cell cycle state, RAP1 was observed with an apparent molecular weight of ~180 kDa, in line
544 with preassembly into the tetrameric form in which it participates to form the octameric
545 TRF2-RAP1 complex composed of four copies of each protein (Arat and Griffith, 2012). In
546 mitotic cells, the strongest peak group containing RAP1 and TRF2 centered around 950 kDa,
547 ca. 2.5x the weight expected for TRF2-RAP1 hetero-octamers, suggesting the association of
548 the octamer with as yet unknown proteins. Notably, RAP1 has been known to associate with
549 the I-kappa-B-kinase (IKK) complex to enhance NF-kappa-B target gene expression (Teo et
550 al., 2010). To test whether the observed 950 kDa signal reflected the RAP1 pool likely
551 engaged in an interaction with the IKK complex, we considered in addition the elution
552 profiles of IKK subunits CHUK and IKKB (**Figure S5A**). The CHUK and IKKB profiles

553 suggest the presence of two distinctly sized and only partly SEC-resolved variants of the IKK
554 complex, one of ca. 2.5 MDa (apex fraction 12) and one of ca. 1.7 MDa (apex fraction 16)
555 (**Figure S5A**). The majority of the RAP1 signal at ca. 950 kDa appeared independent from the
556 two distinct populations of IKK complex variants observed. However, a peak shoulder in the
557 RAP1 signal at elevated molecular weight (estimated apex fraction 16) conformed with a
558 small fraction of RAP1 bound to the 1.7 MDa but not the 2.5 MDa variant of the IKK
559 complex (**Figure S5A,** lower panel, fractions 14-18).

560 As a second example, we observed striking changes in the elution profile of the Nup107-160
561 sub-complex of the NPC (Corum ID 87, **Figure 5H**). All 9 subunits were detected with
562 significant SEC shifts (**Figure 5H**, middle panel). In mitotic cells, the complex was observed
563 based on a co-elution peak group formed by all subunits at a molecular weight of 2.8 MDa
564 (Apex fraction 13, **Figure 5H**, right panel). In interphase cells, no defined co-elution peak
565 was detected in this size range, suggesting the presence of the Nup107-160 sub-complex
566 exclusively in mitotic extracts. Interestingly, the subunit SEC13 was observed in a second
567 peak at ~ 1 MDa in both cell cycle states, suggesting its presence in an additional complex
568 resolved by SEC. We surmised that this peak may represent SEC13 in the context of its
569 alternative functional role in COPII vesicle-mediated transport (Tang et al., 1997). To test this
570 hypothesis, we overlayed the elution profiles of the SEC13 partners in the coatomer complex
571 and, indeed, observe co-elution with its partner SEC31 but not with the adaptor proteins
572 SEC23A/B and SEC24/B (See **Supplemental Figure S6**). These observations demonstrate
573 the capacity of our method to capture mitotic liberation of Nup107-160 sub-complexes from
574 NPCs in and to resolve protein engagement across different functional contexts. Mitotic
575 disassembly of NPCs is a hallmark of mitotic progression (Linder et al., 2017) but this event
576 has not been annotated in the respective GO terms. This insight into complex dynamics at
577 sub-complex resolution led us to explore whether SEC-SWATH-MS chromatographic
578 profiling could reveal further and potentially novel aspects of mitotic NPC disassembly (see
579 below).

580 In summary, these results show that a major portion of the proteome changes at the level of
581 complex association between mitotic states and that hundreds of specific complex remodeling
582 events were apparent from the data. Insights at sub-complex resolution warrant in-depth
583 analysis of chromatographic profiles not only for newly implicated proteins but may also
584 reveal novel or additional roles of proteins with known functions in cell cycle progression.

585

586 *Figure 5: Inference of cell-cycle dependent complex remodeling.* **A** Global proteome assembly states observed in
587 interphase and mitosis. Bar plots show numbers of proteins eluting in one to five distinct peaks. Pie charts show

588 that the majority of proteins peak at least once in the likely complex-assembled range (apparent molecular
589 weight twice or larger than the annotated monomer molecular weight). In either cell cycle state, 12% of the
590 proteins are observed in both monomeric and complex-assembled state and ca. 30 % of the proteins elute in two
591 or more distinct peaks, in line with previous observations on the HEK293 proteome modularity profiled by SEC-
592 SWATH-MS (Heusel, Bludau et al., 2019). Peak detection was strictly error-controlled (q-value FDR estimate of
593 5 %) against randomized peptide-to-protein associations. For details, see experimental procedures. **B** Preferential
594 detection of shifts in proteins that are subunits of known reference complexes of the CORUM database displayed
595 based on the proteins SEC shift score ranks. Proteins that under certain conditions integrate into complexes
596 display lower ranks, with rank 1 representing the highest SEC shift score observed. **C** Coverage of CORUM
597 reference complexes in SEC-SWATH-MS. Upper chart: Coverage on the level of complex component subunits.
598 Lower chart: Coverage on the level of complexes (covered if two or more of the annotated subunits were among
599 the SEC-SWATH-MS results). **D** The 949 complexes covered in the dataset with two or more subunits. For
600 visualization purposes, the complexes are represented by the complex-level means of subunit-level differential
601 SEC shift scores. **E** The 432 complexes that were detected to undergo remodeling in mitosis vs. interphase,
602 based on significant SEC shifts of minimally two of their component subunit proteins. For visualization
603 purposes, the complexes are represented by the complex-level means of subunit-level differential SEC shift
604 scores. The coloring indicated whether the complex is annotated with "cell cycle" in the database-contained gene
605 ontology terms (GO). **F** For the changing complexes, the fraction of shifting subunits (of those detected by SEC-
606 SWATH-MS) was plotted as function of complex size (n subunits, detected by SEC-SWATH-MS) and whether
607 or not the complex bears the GO annotation 'cell cycle'. Shift completeness is higher among cell cycle-related
608 assemblies. **G** Example of a complex that is remodeling along the cell cycle states but not annotated with 'cell
609 cycle', TRF2-Rap1 complex III (CORUM ID 1205), showing a representative spokes model, subunit protein
610 level SEC-shift scores in the context of all observed shift scores and their quantitative elution along SEC as
611 profiled by SWATH-MS. Both subunits display significant SEC shifts. The analysis detects a co-elution signal
612 indicating the presence of a complex of ca. 950 kDa (Apex fraction 21) in mitosis but not in interphase, where
613 only RAP1 is detected. **H** Equivalent to panel G. Second example of a complex that is remodeling along the cell
614 cycle states but not annotated with 'cell cycle', Nup107-160 subcomplex (CORUM ID 87), showing a
615 representative spokes model, subunit protein level SEC-shift scores in the context of all observed shift scores and
616 their quantitative elution along SEC as profiled by SWATH-MS. All 9 subunits display significant SEC shifts.
617 The Nup107-160 sub-complex appears specifically in mitosis and with an apparent molecular weight of 2.8 MDa
618 (Apex fraction 13, right panel). Subunit SEC13 shows an additional peak at ca. 10 MDa (Apex fraction 20-21)
619 where it appears bound to its partner subunit in its alternative context in the COPII complex, SEC31
620 (**Supplemental Figure S6**).

621 ## Discovery and independent validation of NPC disassembly intermediates

622 The discovery of compositional rearrangements of protein complexes between cell cycle
623 states allowed us to propose testable changes of biochemical processes. Among these is the
624 mitotic disassembly of the NPC (Hoelz et al., 2016). The ensemble of SEC protein profiles
625 analyzed in this study contained 27 of the 32 bona fide NPC components (Hoelz et al., 2016),
626 shown in **Figure 6A** in either state. The patterns show a general, distinctive change towards
627 complexes of lower MW in the mitotic sample, consistent with NPC disassembly into sub-
628 complexes. All but one of the detected subunits (NUP50) showed shifts in protein-centric
629 differential scoring. For eight of the subunits, elution peaks in the monomeric range were
630 detected, equally across both cell cycle states. The observation of monomeric pools in the
631 SEC experiment may indicate the presence of a subset of NPC components that seem to be
632 present in the cell as assembly-competent monomeric forms, to potentially bind other partners
633 to fulfill other functions or liberated from partner Nups during preparation of the cell extracts.

634 Due to the distinctive pattern changes between the two states tested, we focused on the key
635 inner ring complex component NUP93, which functions as an adaptor between the NPC
636 scaffold and the central channel FG Nup62-Nup58-Nup54 sub-complex. In interphase
637 extracts, NUP93 was principally detected in a wide high MW peak (fractions 1-15, > 10 MDa
638 to ca. 1.8 MDa) apart from minor amounts detected in two lower MW populations (apex
639 fraction 29, ~ 360 kDa and apex fraction 37, ~145 kDa). In the mitotic state, NUP93 was
640 detected in three distinct lower MW SEC peaks, with a new signal at an apparent MW of ca.
641 570 kDa (elution range F21-F27) and two signals of increased intensity when compared to the
642 interphase pattern at apparent MW of ca. 320 kDa (elution range F27-F33) and 145 kDa
643 (elution range F35-F39) (**Figure 3F**, **Supplemental Figure S5B** and schematically illustrated
644 in **Figure 6B**). The observed peak pattern indicates that in mitotic cells NUP93 associates
645 with complexes of different size that elute markedly earlier than monomeric NUP93 (93.5
646 kDa, expected elution fraction 41), thus suggesting the formation of distinctive NUP
647 disassembly intermediates containing NUP93. To infer the composition of these complexes,
648 we locally correlated the elution pattern of NUP93 with the elution patterns of other Nups
649 (**Figure 6B**). For the peak at ca. 320 kDa, this analysis suggested NUP205, NUP155 and
650 NUP214 as NUP93 interaction partners (F27-33, **Figure 6B**, right panels). Similarly, for the
651 peak at ca. 570 kDa, (**Figure 6B** left panel), six proteins, namely the central channel FG Nups
652 NUP62, NUP54 and NUP58 as well as NUP188, NUP50 and TPR eluted in the same peak as
653 NUP93.

654 The relative mass spectrometric signal intensities of peptides can be used to estimate the
655 abundance of a protein in a SEC peak (Ludwig and Aebersold; Rosenberger et al., 2014**).** For
656 the peak at ca. 320 kDa quantification of the respective protein signal intensities identified the

657 inner ring proteins NUP155 and NUP205 as the predominant binding partners of NUP93. In
658 contrast, NUP214, whose quantitative pattern correlates well in the SEC dimension, is present
659 at much lower signal intensity which is not consistent with stoichiometric participation in the
660 complex. The results thus suggest a complex dissociating from the NPC holo-complex in
661 mitosis that is composed of NUP93, NUP155 and NUP205. Notably, NUP188 displays only
662 low local correlation with NUP93 in the queried target range, suggesting that NUP188 does
663 not participate in the complex of ~320 kDa detected between F27 and F33 (**Figure 6B**, right
664 panel). The observed MW of 320 kDa is smaller than the cumulative weight of a
665 stoichiometric hetero-trimer (476 kDa). This discrepancy could be due to compact shape
666 and/or interactions with the stationary phase. Similarly, we used the protein intensities to also
667 estimate composition and the abundances of the proteins in the peak at ca. 570 kDa (**Figure**
668 **6B** left panel). The data suggest that in this complex the inner ring component NUP93 was
669 associated with the central channel sub-complex NUP62, NUP54 and NUP58, as well its
670 inner ring complex partner subunit NUP188. Based on the absolute signal intensity,
671 stoichiometric participation of TPR in the ~570 kDa assembly appears unlikely. These
672 findings are supported by current models of NPC structure (Beck and Hurt, 2017; Hoelz et al.,
673 2016; Lin et al., 2016) in which central channel Nups are coordinated by adaptor Nups of the
674 inner ring complex. Based on the holo-complex model, the recovery of both TPR and NUP50
675 as part of NUP93-containing complexes appears unlikely, whereas interaction between
676 NUP93 and central channel appears probable because NUP93 serves as anchor point for the
677 central channel within the NPC holo-complex (Chug et al., 2015; Hoelz et al., 2016; Lin et al.,
678 2016).

679 We validated the existence of the previously unknown mitotic sub-complex consisting of
680 NUP93, NUP188 and the trimeric central channel sub-complex NUP62-NUP58-NUP54 by
681 co-precipitation coupled to immunoblotting or mass spectrometry as orthogonal methods. We
682 inducibly expressed HA-St-tagged NUP58 in HeLa cells synchronized in either interphase or
683 mitosis. As a control for the completeness of mitotic arrest, we performed immunoblots of
684 NUP53 in the input samples, demonstrating its efficient mitotic hyper-phosphorylation, as
685 previously reported (Linder et al., 2017). We isolated the native complex associated with the
686 tagged Nup58 under mild conditions and tested the isolate for the presence of the suggested
687 complex components by immunoblotting and LC-MS/MS in either cell cycle state (**Figure**
688 **6C&D** , **Supplemental Figure S1D&E)**. Indeed, immunoblotting confirmed co-purification
689 of both the immediate partner Nups (NUP62, NUP54) and the inner ring complex components
690 NUP93 and NUP188 with NUP58 from interphase cells. Importantly, in mitosis, this
691 connectivity was maintained, in agreement with our SEC-SWATH-MS results (**Figure 3C**).
692 These data confirm the presence of a mitotic sub-complex involving both central channel and

693 inner ring complex components NUP93 and NUP188. The observed relative signal intensities
694 in immunoblotting show a reduced recovery of NUP93 with the central channel Nups in
695 mitosis compared to interphase. This is consistent with mitotic partitioning of the NUP93
696 protein pool across multiple macromolecular entities, as indicated by SEC-SWATH-MS
697 (**Figure 3C**, rightmost two lanes and compare **Figure 6B**, right panel).

698 Next, we analyzed proteins co-isolated with Nup58 by mass spectrometry and used the
699 number of identified mass spectra as semi-quantitative measure to estimate protein retrieval
700 from cells in either cell cycle state and respective controls. The results further confirmed the
701 co-purification of NUP93 and NUP188 and also showed the presence of the inner ring
702 complex component NUP205 (**Figure 6D**). Notably, NUP205 was consistently detected in the
703 SEC elution range under investigation (F21-F27) but did not show a distinctive co-elution
704 peak. Neither NUP50 nor TPR were detected as significant components of the isolates and are
705 unlikely to represent *bona fide* components of the new sub-complex. (**Figure 6D**). Thus,
706 Nup50 is likely part of a different, independent protein complex eluting at a similar position
707 in SEC, which can motivate future research on the mitotic fate of this Nup.

708 Together, these results indicate that, in contrast to preceding models of NPC disassembly, a
709 fraction of the inner ring complex components NUP93 and NUP188 and likely NUP205
710 remain attached to the central channel sub-complex composed of NUP62, NUP58 and NUP54
711 after mitotic entry. This configuration can explain how central channel Nups are efficiently
712 reincorporated into reforming NPCs along with their partner scaffold Nups during mitotic
713 exit. Further, a second population of NUP93 is stored in a mitotic sub-complex with the
714 canonical IRC components NUP155 and NUP205 in absence of NUP188 (See model in
715 **Figure 6E**).

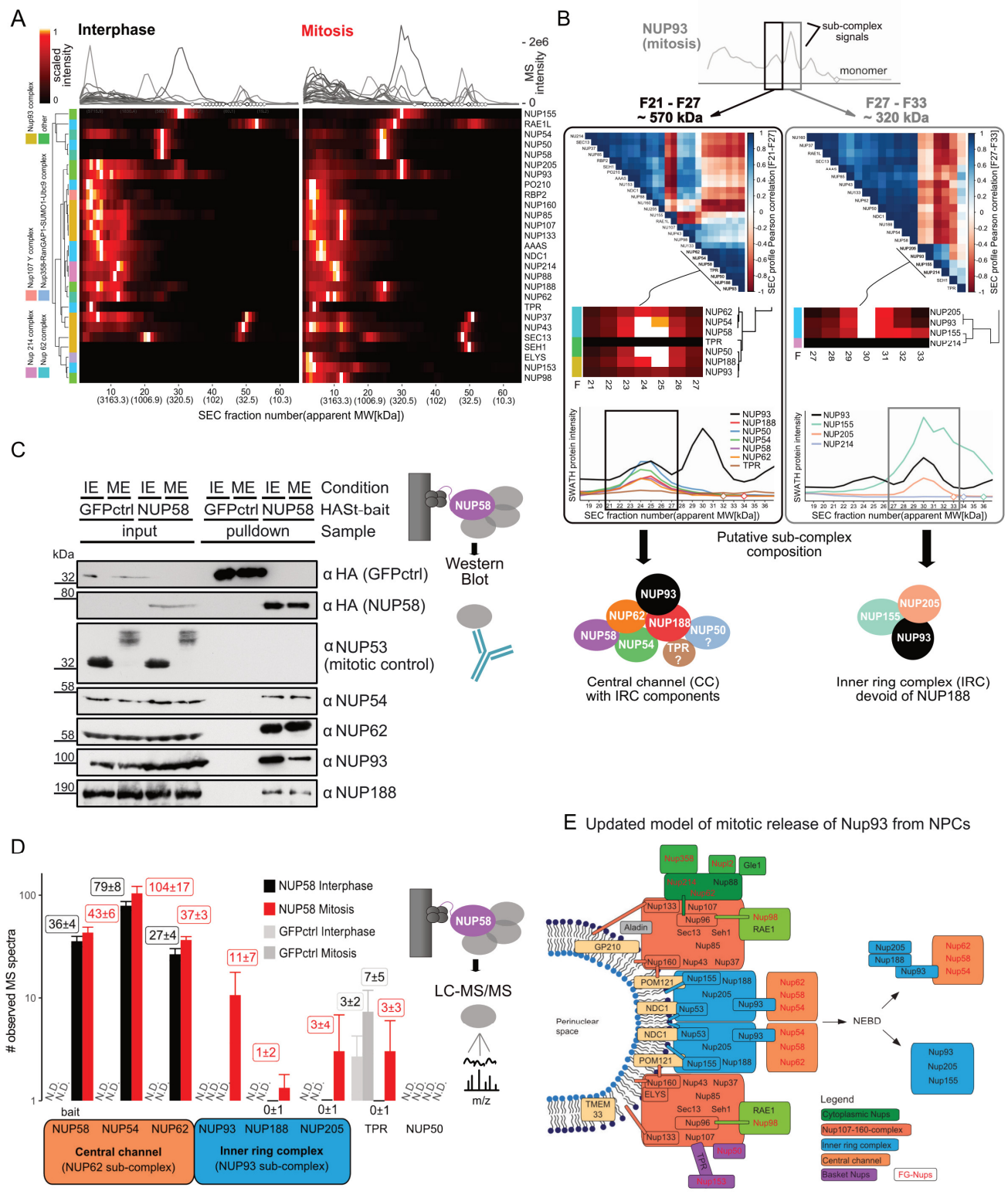

716

717 *Figure 6: Discovery and independent validation of NPC disassembly intermediate.* **A** Quantitative elution
718 patterns of NPC subunits in interphase and mitosis display protein mass re-distribution from large nucleoporin
719 complexes in interphase with void volume elution (> 5MDa) towards lower MW ranges larger than individual
720 components, in line with NPC disassembly into defined sub-complexes. Also compare Figure 3F. **B** Targeted
721 search for co-eluting proteins as candidate co-complex members, using as basis two of the mitotically induced
722 sub-complex signals arising from the inner ring complex component NUP93. Left panel: MS signal correlation
723 analysis in the first peak (apex fraction, 25; apparent MW, ca. 570 kDa; elution range, F21-F27) nominates
724 candidate members of the sub-complex eluting in signal 1 based on co-elution. Right panel, co-elution-based

725 nomination of additional sub-complex membership candidates for signal 2 (apex fraction, 30; apparent MW, 320
726 kDa; elution range F27-F33). Bottom, putative sub-complex composition subjected to validation experiments
727 (see panels C&D). Note that targeted search for co-eluting proteins (on global dataset scale) is a core function of
728 our online data interrogation tool SECexplorer-cc. **C** Testing mitotic sub-complex composition based on co-
729 purification with central channel complex captured via NUP58 by immunoblotting. As mitotic control NUP53
730 was included and complete size shifts indicate high homogeneity of cell cycle state of the analyzed cell
731 populations in interphase (IE) and mitosis (ME). As negative control to control for non-specifically bound
732 background protein, green fluorescent protein was included. Both NUP93 and NUP188 co-purify with the
733 central channel in interphase and continue to do so in mitosis, confirming the results from SEC-SWATH-MS. **D**
734 Testing mitotic sub-complex composition based on co-purification of Nups with the central channel complex
735 captured via NUP58 by mass spectrometry (AP-MS). The number of identified mass spectra serves as semi-
736 quantitative measure to estimate protein retrieval from cells in either cell cycle state and respective controls. The
737 results confirmed the co-purification of NUP93 and NUP188 and also showed the presence of the inner ring
738 complex component NUP205. which is detected in SEC but does not form a defined elution peak in the signal 1
739 range. Neither TPR nor NUP50 are recovered in amounts above background binding level and are thus likely not
740 part of the mitotic NPC sub-complex. **E** Model of mitotic NPC disassembly and storage of NUP93 in distinct
741 mitotic sub-complex reservoirs before re-formation of daughter cell nuclear envelopes. A substantial fraction of
742 NUP93 is stored in the newly identified mitotic sub-complex composed of central channel components NUP54,
743 NUP58 and NUP62 as well as inner ring complex components NUP93, NUP188 and NUP205.

744 Browsing dynamic complex association maps in SECexplorer-cc

745 SEC-SWATH-MS portrays the process of mitosis from the angle of protein mass re-
746 distribution across differently sized stable complexes resolved by SEC. There remains a lot to
747 be learned from the rich dataset generated, with the prospect of discovering new proteins
748 involved in cell cycle regulation and of identifying new components of both static as well as
749 dynamic assemblies. To support community-based mining and interpretation of our dataset,
750 we provide a web tool, *SECexplorer-cc* (https://sec-explorer.shinyapps.io/hela_cellcycle/,
751 **Figure 7**) which offers four functionalities: (i) Interactive viewing of protein SEC
752 fractionation profiles in interphase and mitosis (compare **Figure 3D** and **F**). (ii) Search for
753 locally co-eluting proteins to identify putative new binding partners showing strong co-elution
754 within a certain range of target protein elution (compare **Figure 6B**). (iii) Interactive display
755 and protein selection from the differential association score map (compare **Figure 3A**). (iv)
756 Display of one or multiple protein's fractionation profiles in reference to the profiles of
757 immediate interaction and/or functional partners dynamically retrieved from StringDB
758 (Szklarczyk et al., 2017). We expect that *SECexplorer-cc* will support a community effort to
759 fully leverage the rich information encoded by the mitotic proteome rearrangement SEC-
760 SWATH-MS data, which, ideally, will support better understanding of modular proteome
761 function along cell division.

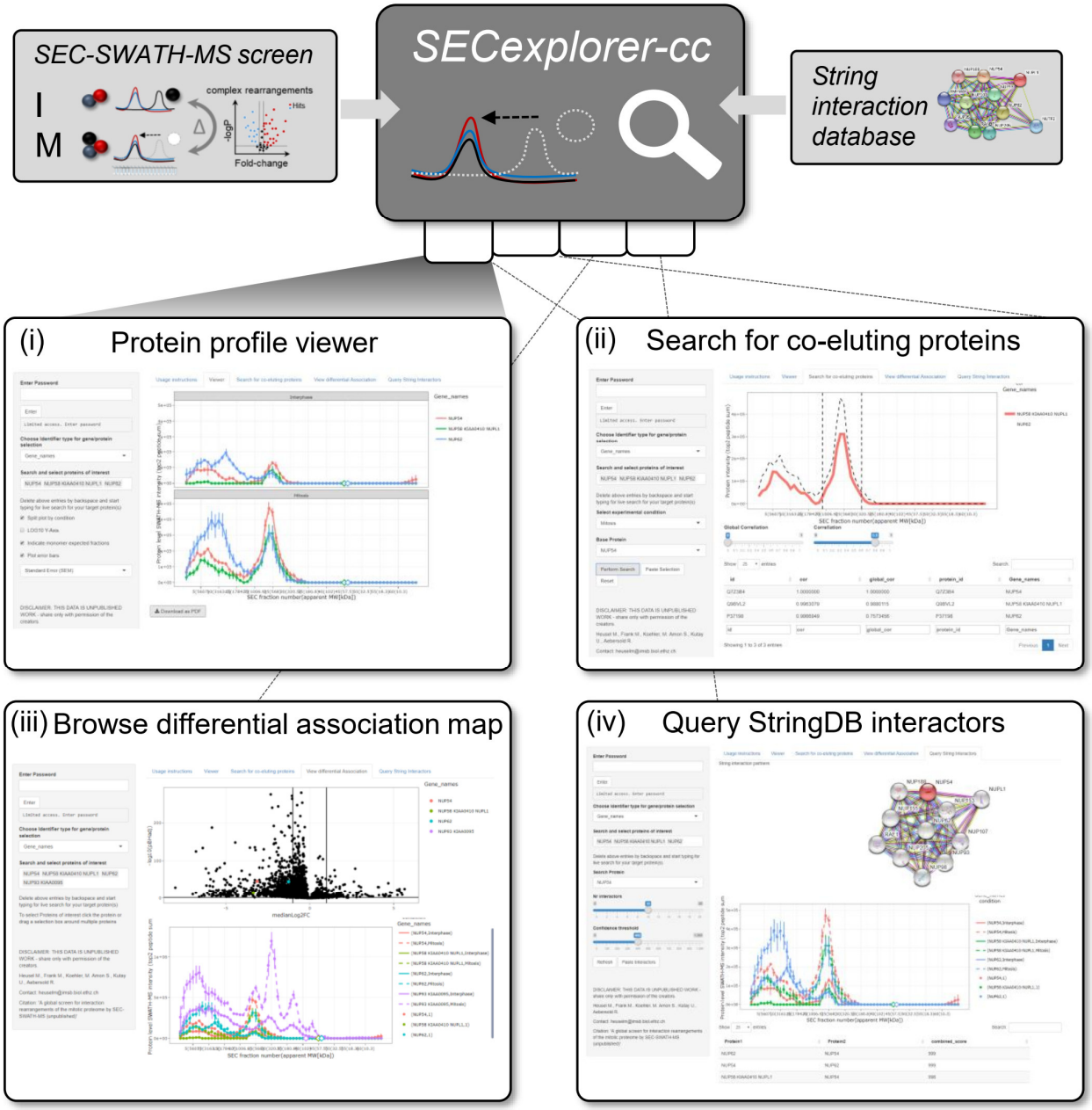

Figure 7: Browsing dynamic complex association maps in SECexplorer-cc. Overview of *SECexplorer-cc*, a web tool that allows to browse and rapidly interrogate differential SEC-SWATH-MS datasets to support researches in customized hypothesis testing. SECexplorer-cc currently combines the dynamic cell-cycle proteome association map reported here and integrates it with information from the String database (Szklarczyk et al., 2017). *SECexplorer-cc* features four core functionalities. **(i)** Interactive display and hit protein selection from the statistical SEC shift score map. **(ii)** Semi-targeted search for locally co-eluting proteins to identify putative new binding partners showing strong co-elution within a certain range of target protein elution. **(iii)** Display of custom protein sets conditional fractionation profiles. **(iv)** Display of one or multiple hit protein's fractionation profiles in reference to its immediate functional and/or physical interaction partners obtained StringDB to discover potential physical association among functionally related proteins and to add cellular context information.

774 # Discussion

775 The biochemical state of a cell is the result of the ensemble of biochemical functions which in
776 turn are largely carried out by macromolecular complexes. Changes in the quantity,
777 composition, subunit topology or structure of such complexes are thus assumed to reflect
778 altered functional states of the cell and the systematic detection of such alterations is therefore
779 of great interest for basic and translational research.

780 In this study we introduce a new software module to the *CCprofiler* suite (Heusel, Bludau et
781 al, 2019) that supports the differential, quantitative analysis of thousands of proteins and their
782 association with complexes from SEC-SWATH-MS datasets, based on a complex-centric
783 analysis strategy. We benchmarked the tool and applied it to detect rearrangements protein
784 complexes in a differential analysis of human cells in two chemically induced cellular states,
785 interphase and mitosis/early prometaphase. The described technique is based on the co-
786 fractionation and protein correlation profiling rationale (Dong et al., 2008; Foster et al., 2006;
787 Liu et al., 2008; Wessels et al., 2009) and includes the improvements with regard to
788 chromatographic resolution, accurate data-independent mass spectrometry (Gillet et al., 2012;
789 Röst et al., 2014) and complex-centric data analysis strategy implemented in SEC-SWATH-
790 MS (Heusel and Bludau et al., 2019). Through the addition of the quantification module, the
791 workflow now supports the systems-wide differential analysis of > 5,000 of proteins and their
792 association with complexes. The data show that the system shows a high degree of
793 reproducibility and performs favorably when benchmarked against protein thermostability
794 measurements, an orthogonal state-of-the-art method to infer changes in protein complexes
795 (Becher et al., 2018; Dai et al., 2018). Application of the method to HeLa CCL2 cells
796 recapitulated known cell cycle-dependent complex remodeling events between the cell cycle
797 states tested and suggested a new model of nuclear pore complex disassembly which was
798 subsequently validated by orthogonal methods, thus demonstrating the potential of the method
799 and dataset to reveal new biology. To support additional exploration of the present data set
800 and future differential SEC-SWATH datasets, we provide an online tool, SECexplorer-cc.

801 To retrieve information on changes in protein complex quantity and composition, we devised
802 a protein-centric differential analysis strategy that detects altered SEC distribution patterns of
803 ca. 5,000 proteins. Changes in these elution patterns between conditions indicated changes in
804 the association of the respective protein with different complexes and such events could be
805 quantitatively compared between states using the new quantification module implementing a
806 strategy we term differential association testing. This computational pipeline was devised to
807 achieve (i) optimal sensitivity to recall changes based on all available peptide-level
808 information and (ii) maximal coverage by not restricting the differential analysis on

809 previously known protein complexes. With more than 90% of the identified proteins being
810 represented as quantitative SEC elution peaks, the method achieved broad coverage of
811 biological functions. The protein-centric differential analysis pipeline is implemented as
812 additional module of our R/CCprofiler toolset, available at
813 https://github.com/CCprofiler/CCprofiler/tree/helaCC).

814 To benchmark the method we compared the differential SEC-SWATH-MS data obtained in
815 this study with results of two studies that investigated cell-cycle-associated changes in protein
816 complexes through inference from protein thermostability changes measured in similarly
817 perturbed cell systems (TPP and CETSA, (Becher et al., 2018; Dai et al., 2018)). The TPP and
818 SEC studies used HeLa cells (TPP; HeLa Kyoto; SEC, HeLa CCL2) and the CETSA study
819 used K562 cells. Under the assumption of strong conservation of the mitotic regulatory
820 circuitry between the cells tested, our comparison suggests favorable sensitivity to recall
821 known cell cycle dependent complex rearrangement events of the SEC-SWATH-MS method.
822 Despite the relatively small overlaps between the protein sets showing strongest mitotic
823 changes in either method (15 - 16 %, see **Figure 4C**), the protein sets largely converged at the
824 level of biological processes and pathways that were associated with the selected protein sets.
825 Our results give first insights into the biological information gleaned from the two
826 approaches, thermal stability and SEC-SWATH-MS, respectively, to infer mitotically altered
827 protein states. However, generic conclusions on the relative merits of detecting alterations in
828 apparent size vs. thermostability of protein complexes are not possible with certainty as in no
829 case the two thermostability-based methods agree on an enriched term that was not also
830 retrieved by SEC-SWATH-MS. More detailed analysis of the approach-specific hits suggests
831 that certain instances of changes in enzymatic and metabolic activities are better-observable
832 based on protein stability rather than size, which could arise from allosteric regulation by
833 small molecule binding which is expected to be better detectable by altered thermostability
834 than by altered complex size. Furthermore, the measurement of thermostability via TPP
835 showed smaller bias against capturing of changes in membrane- and DNA-associated proteins
836 than the results from the SEC-SWATH-MS and CETSA workflows (**Figure 4D**). Overall our
837 comparison indicates higher sensitivity of the SEC-SWATH-MS method to uncover changes
838 in core cell cycle machinery (**Figure 4E**), such as e.g. increased formation of translation
839 initiation complexes or the inactivation of APC/C complex (**Supplemental Figure S3A**),
840 when compared to the stability-based approaches. Overall the data suggest that SEC, as
841 implemented in the SEC-SWATH-MS workflow, currently offers a preferable combination of
842 analytical breadth and sensitivity.

843 Our study generated new and confirmed known biological insights. For example, only a
844 subset of the CDK1 pool is recruited to upregulated CCNB1 in mitosis (31% appear to remain

845 monomeric, compare **Figure 3D**). This effect cannot be attributed to incomplete
846 synchronization of the analyzed cell populations. We surmise that the degree of assembly acts
847 as an additional layer of CDK1 activity control by defining the cellular concentration of
848 assembled CCNB1-CDK1 complexes that can be transferred to an active state by protein
849 phosphorylation (Nigg, 1993). This notion is relevant for ongoing drug development
850 programs that target the respective interaction interfaces as alternative anticancer strategy
851 (Peyressatre et al., 2015).

852 Differential SEC-SWATH-MS data also illustrated the process of mitotic disassembly of
853 NPCs into distinctive sub-complexes. This allowed us to identify a novel mitotic sub-complex
854 and to extend the model for mitotic NPC disassembly (Laurell et al., 2011; Linder et al.,
855 2017). These observations from the SEC-SWATH dataset were further confirmed with
856 orthogonal methods. Even though several publications reported mechanistic insights into the
857 phosphorylation-driven process of mitotic NPC disassembly (Laurell et al., 2011; Linder et
858 al., 2017), the overall process remains incompletely understood. NPC disassembly must
859 liberate Nups in a state in which they are readily available for rapid reassembly during mitotic
860 exit. Our discovery of a mitotic protein complex between central channel FG-Nups and their
861 anchoring scaffold Nups indicates that the efficient incorporation of the FG Nups may occur
862 together with their anchoring partners. Such mechanism would be ideally suited to explain
863 correct and rapid reassembly during mitotic exit. In this scenario, reintegration will rely on a
864 larger set of protein interactions directed by the scaffold subunits. Detailed knowledge about
865 the mechanistic rules of mitotic NPC disassembly and interphasic re-assembly may well
866 prove helpful in the design of future therapies aiming to modulate the process of cell division.

867 The specific complexes discussed in this paper, including the novel NPC disassembly
868 intermediates only represent a small fraction of the information contained in the dataset of
869 5,044 proteins of which 1,793 showed significantly different association with complexes
870 across the two cell cycle states analyzed. To support further in depth interrogation of the
871 dataset we disseminate it in an easily browsable form via *SECexplorer-cc*. To infer strong
872 hypotheses on novel players that justify at times costly and lengthy follow-up experiments, it
873 is important to bear in mind inherent limitations of and potential confounding effects in the
874 experimental system. These include i) differential extractability of proteins due to cellular re-
875 organization, exemplified by breakdown of the nuclear envelope upon mitotic entry, ii)
876 indirect effects, i.e. rearrangement as a mere consequence rather than cause of the altered state
877 of the biological system, iii) confounding effects of the experimental procedure, such as e.g.
878 stress responses triggered by chemical treatment rather than cell cycle stage, as has been
879 suggested in comparisons of quantitative proteome profiles employing different protocols to
880 achieve cell cycle synchronization (Ly et al., 2015). Further, co-elution may be observed

881 among proteins that participate in physically independent complexes that co-elute in
882 chromatography, as exemplified by NUP50 co-elution with but not participation in the newly
883 identified mitotic NPC sub-complex reported here. Further, experimentally induced
884 disassembly of labile complexes is expectable under SEC-induced dilution and will likely
885 result in an overestimation of the proteins present in monomeric form.

886 Multiple extensions or optimizations of the SEC-SWATH-MS methodology can be
887 envisioned. For example, given the diverse properties of cellular assemblies methodological
888 adaptations could benefit more focused studies of a given complex class of interest, such as
889 e.g. ribosomal complexes (Yoshikawa et al., 2018). Further, limited sample throughput of the
890 method currently precludes time course or cohort analyses (Compare 473 LC-MS
891 measurements and 556 hours of gradient time spent here), a bottleneck which may be
892 bypassed by integrating ultra-fast liquid chromatography setups (Bache et al., 2018) in the
893 SWATH/DIA-MS workflow. Such adaptations will likely render the analysis of proteomes
894 including their organizational state a routine procedure in the near future.

895 Another thrust for further development of the method is bioinformatic information retrieval.
896 We here deliberately chose an approach that makes use of all peptide level information to
897 detect rewiring proteins with maximal sensitivity and at optimal breadth. However, alternative
898 computational strategies can be envisaged that will support the retrieval of additional
899 information from SEC-SWATH-MS data. These include (i) increased sensitivity to detect
900 proteins that exchange interactors without effect on the SEC-SWATH-MS signal (net-0
901 interactome changes) by interaction-network-centered approaches, (ii) improved method
902 throughput by reducing the need for replication and rate of SEC sampling, (iii) improved
903 information retrieval on the level of protein complexes and their precise composition across
904 functional states and (iv) retrieval of information on post-translationally modified and
905 alternatively spliced gene products and the respective impact on complex assembly and
906 dynamics thereof. With developments along those lines ongoing, it appears particularly
907 promising to re-interrogate the SEC-SWATH-MS data presented here from these additional
908 perspectives in the future.

909 In contrast to classical proteomics studies that reduced proteomes to a quantitative list of
910 component parts, SEC-SWATH-MS facilitates studies of the proteome including its
911 biophysical arrangement into complexes as a core functional layer. This enables deep,
912 systems-wide surveys of changes in protein association- and inferred activity states from
913 virtually any experimental system of interest as the method is independent from genetic
914 engineering. The datasets encode protein assembly and interaction states, the composition of
915 complexes and alternate roles of distinct proteoforms. Systematic measurements of protein

attributes closely correlated to protein function bear profound potential for the discovery of yet unknown players and mechanisms at the core of (disease) phenotypes generated by biomolecular networks and systems.

Acknowledgments

We would like to thank the Scientific IT Support (ID SIS) of ETH Zurich for support and maintenance of the Aebersold lab-internal computing infrastructure and the ScopeM facility for continuous support of microscopy at ETH Zurich. The project was supported by the SystemsX.ch projects PhosphoNetX PPM and project TbX to R.A., the Swiss National Science Foundation (grant no. 3100A0-688 107679 to R.A. and 310030_184801 to U.K.), and the European Research Council (ERC-20140AdG 670821 to R.A. and ERC AdG grant NucEnv_322582 to U.K). M.G. acknowledges the support by the Innovative Medicines Initiative project ULTRA-DD (FP07/2007-2013, grant no. 115766). MH was supported by a grant from Institut Mérieux. B.C.C. was supported by a Swiss National Science Foundation Ambizione grant (PZ00P3_161435).

Author Contributions

Conceived and supervised project, UK, BCC, MG and RA; Performed experiments, MK, SAm, FF and MH, Generated and characterized the HeLa cell line expressing tetracycline-inducible HA-Strep Nup58, MIL, Performed data analysis, MF, MH, SAu; Developed and implemented data analysis tools MF, MH, IB, GR; Writing – original draft, MH; Writing – review & editing, MF, MK, SAm, GR, FF, IB, SAu, BCC, MG, UK, RA.

Declaration of Interests

The authors declare no conflict of interest.

Figure Titles and Legends

To ease review upon initial submission, the following figures including legends have been interspersed in the results section:

Figure 1: Proteome rearrangement screening by SEC-SWATH-MS: Workflow and dataset properties.

Figure 2: Proteome rearrangement screening by SEC-SWATH-MS: Data acquisition and processing.

Figure 3: Benchmarking part 1: Recall of expected mitotic complex remodeling events.

946 Figure 4: Benchmarking part 2: Performance of measuring proteome state dynamics by
947 apparent size vs. thermostability.

948 Figure 5: Inference of cell-cycle dependent complex remodeling.

949 Figure 6: Discovery and independent validation of NPC disassembly intermediates.

950 Figure 7: Browsing dynamic complex association maps in SECexplorer-cc.

951 Tables

952 There are no main text tables. All tables related to our work are included in the form of
953 supplemental tables (See Supplemental Information).

954 Experimental Procedures (initial submission)

955 Cell culture and mitotic arrest

956 HeLa CCL2 cells were obtained from the ATCC collection and cultured in modified complete
957 Dulbecco Modified Eagle Medium (DMEM) at 37°C and 5% CO2. Cells in interphase (early
958 S-phase) were obtained by double-thymidine block. Cells in mitosis (early prometaphase)
959 were obtained by single thymidine block followed by nocodazole treatment and mitotic
960 shake-off, as follows. Cells were grown to a confluency of approximately 60% and arrested in
961 S phase by addition of 3 mM thymidine (Sigma) for 20 h. After overnight incubation the cells
962 were thoroughly washed twice with warm PBS and left for recovery in complete DMEM
963 medium for 2 h prior to addition of 3 mM thymidine (Sigma) and incubation at 37°C for 13 h
964 (interphase-arrest by double thymidine-block), or, for synchronization in mitosis, cells were
965 treated with 100 ng/ml nocodazole at 37°C for 13 h before harvest via mitotic shake-off to
966 ensure recovery of only mitotic cells. Cells arrested in interphase were harvested using
967 EDTA, before cells were pelleted and snap-frozen in liquid nitrogen. Synchronization in
968 interphase and mitosis was confirmed by monitoring phosphorylation of NUP53 by Western
969 blotting and the observed weight gain of mitotic, poly-phosphorylated NUP53 (See **Figure**
970 **3C** and **Figure S1A**).

971 Tandem affinity purification of central channel complexes

972 HeLa cell lines carrying tetracycline-inducible HA-Strep-tagged NUP58 and HA-Strep-
973 tagged GFP were generated using a HeLa Flp-In T-REx cell line (Häfner et al., 2014).
974 Expression of HASt-NUP58 and HASt-GFP were induced by addition of 0.1 µg/mL
975 tetracycline (Sigma). Correct expression and localization of affinity-tagged Nup58 was
976 validated by immunofluorescence and Western blotting (see below). For affinity purifications,
977 bait expression was induced for 48 h before synchronizing the cells in interphase or
978 prometaphase as described above. After washing and pelleting, cells were snap-frozen in

979 liquid nitrogen. Thawed cells were lysed by resuspension in lysis buffer containing 25 mM
980 Tris-HCl pH 7.6, 125 mM NaCl, 2 mM MgCl2, 1 mM DTT, 0.5% NP-40, protease and
981 phosphatase inhibitors and sonicated. After lysate clearance by centrifugation (15'000 rpm, 30
982 min, 4°C), HA-Strep-Nup58 and HA-Strep-GFP were purified by affinity chromatography
983 with StrepTactin sepharose (IBA) for 45 min at 4°C. Beads were washed three times with
984 lysis buffer and one time with lysis buffer without NP40 and protease inhibitors. Bound
985 protein was eluted with elution buffer containing 25 mM Tris-HCl pH 7.6, 125 mM NaCl, 2
986 mM MgCl2, 1 mM DTT and 2.5 mM D-biotin (Sigma). Elutions and input samples were
987 further analysed using SDS-PAGE followed by Western blotting.

988 ## Western Blotting

989 Cell pellets from synchronized HeLa CCL2 cells and samples from pulldown experiments
990 were resuspended in SDS-sample buffer and briefly denatured at 95°C. Protein was resolved
991 by SDS-PAGE and transferred to nitrocellulose blotting membranes (GE Healthcare).
992 Membranes were blocked over night with 5% skim milk powder in PBS-T (PBS containing
993 0.1% Tween 20). Subsequently, membranes were incubated at RT for 1 h with indicated
994 antibodies diluted in 5% milk-PBS-T. Primary rabbit polyclonal antibodies directed against
995 NUP188, NUP93, NUP53 and NUP54 have been described (Linder et al., 2017). Antibodies
996 directed against actin (Sigma, cat no. A1978), HA (Roche), pH3 (Cell signaling, cat no.
997 9701S) and NUP62 (Abcam, cat no. ab188413) are commercially available. After three
998 washing steps with TBS-T secondary antibody solutions were applied in 5% milk-PBS-T and
999 membranes kept shaking for 1 h at RT. Subsequent washing was followed by detection. HRP-
1000 conjugated secondary antibodies used to detect primary antibodies included goat anti–rabbit
1001 IgG and goat anti-mouse IgG (Sigma-Aldrich). Chemiluminescence was initiated using ECL
1002 detection reagent (GE Healthcare) and the signal was detected using Fuji RX film (Fujifilm)

1003 ## Validation of cell cycle arrest and HASt-NUP58 HeLa cell line by
1004 immunofluorescence

1005 For immunofluorescence, cells were fixed with 4% paraformaldehyde in PBS, washed with
1006 PBS and permeabilized for 5 min in 0.1% Triton X-100. Immunostaining was performed as
1007 described previously(Zemp et al., 2009). Briefly, cells were blocked with blocking solution
1008 (2% BSA in PBS) at RT for 45 min. Anti-HA antibody (Enzo) was 1:500 diluted and anti-p-
1009 Histone H3S10 (Cell Signalling Technology) 1:400 in blocking solution and fixed cells were
1010 exposed at RT for 1 hr. Subsequently, cells were washed with blocking solution and stained
1011 with fluorescently labelled secondary antibody at a dilution of 1:300. After three washing
1012 steps with blocking solution, DNA was stained using Hoechst 33342 (ThermoFisher) 1:5000
1013 diluted in blocking solution. Eventually, coverslips were mounted in Vectashield mounting

1014 medium (Vector laboratories Inc.) on a glass slide. Localization and expression levels were
1015 analysed using a Zeiss LSM 880 upright microscope with a 63x 1.4NA, oil, DIC Plan-
1016 Apochromat objective, and Western blotting respectively.

1017 Preparation of native proteomes and fractionation for MS analysis

1018 Ca. 5e7 HeLa CCL2 cells were mildly lysed by freeze-thawing into 0.5% NP-40 detergent-
1019 and protease and phosphatase inhibitor containing buffer, essentially as described(Collins et
1020 al., 2013), albeit without the addition of Avidin. Lysates were cleared by 15 minutes of
1021 ultracentrifugation (100,000×g, 4 °C) and buffer was exchanged to SEC buffer (50 mM
1022 HEPES pH 7.5, 150 mM NaCl) over 30 kDa molecular weight cut-off membrane at a ratio of
1023 1:25 and concentrated to 25-35 mg/ml (estimated by OD280). After 5 min of centrifugation at
1024 16,900 ×g at 4 °C, the supernatant was directly subjected to fractionation on a SRT-C-SEC
1025 500 column (dimensions 300×21.2 mm, pore size 500 Å, particle size 5 µm, Sepax-Tech, DE,
1026 USA). Per SEC run, 7.25 mg of native proteome extract (estimated by OD280) was injected
1027 and fractionated at 2 ml/min flow rate on ice (0-4 °C), collecting 90 fractions at 0.4 min per
1028 fraction from 20 to 56 min post-injection, fractions 1-65 (20 – 46 min elution time, 40 – 92 ml
1029 elution volume) of which were considered relevant proteome elution range and considered for
1030 quantitative analysis. For library generation purposes, a few fractions from an extended
1031 elution range were analyzed (up to fraction 89). In order to minimize time-sensitive artifacts
1032 of complex disassembly under dilution, samples were processed independently to achieve a
1033 fixed processing time-to-column of 1.5-2 h. Apparent molecular weight per fraction was log-
1034 linearly calibrated based on the apex elution fractions of a 5-protein standard sample with
1035 known protein mass analyzed with each experimental replicate (Column Performance Check
1036 Standard, Aqueous SEC 1, AL0-3042, Phenomenex, CA, USA). An aliquot of the
1037 unfractionated mild proteome extract was included in peptide sample preparation and LC-MS
1038 analysis.

1039 MS sample preparation

1040 Size exclusion chromatographic fractions and an aliquot of the unfractionated mild proteome
1041 extract were processed as follows. Proteins were denatured by the addition of 1% sodium
1042 deoxycholate (SDC, Sigma-Aldrich) and heating to 95 °C for 5 min. Disulfide bonds were
1043 reduced by adding tris-(2-carboxyethyl)-phosphine to 5 mM and incubating at 37 °C for 30
1044 min. Subsequent alkylation of free thiol groups was carried out by adding iodoacetamide to 10
1045 mM and incubating in the dark for 30 min. Proteins were digested by 1.4 µg sequencing grade
1046 trypsin (Promega) per fraction at 37 °C overnight. 1% TFA and 1% ACN were added for
1047 stopping the digestion and precipitating SDC. Additionally, 0.4 pmol of E. coli β-
1048 galactosidase digest were added as internal standard, followed by centrifugation at 4,500 ×g

1049 for 15 min. Subsequently, samples were desalted by means of C18 reversed phase well plates
1050 (96-Well MACROSpin Plate, The Nest Group, MA, USA) according to the manufacturer's
1051 recommendations and vacuum dried. For MS analysis, de-salted peptide samples were re-
1052 suspended in 20 µl LC solvent A (2% ACN, 0.1% FA) supplemented with internal retention
1053 time calibration peptides (iRT kit, Ki-3002-1, Biognosys AG, CH, used at 1:20 instead of
1054 1:10 ratio as indicated in the manufacturer's protocol).

1055 Tandem affinity purified samples were processed as follows. To remove biotin, proteins were
1056 precipitated from the AP eluate by 25% TCA at -20°C overnight and protein pellets were
1057 washed three times with ice-cold acetone and dried. Proteins were denatured by dissolution in
1058 30 µl of 8M urea in 100 mM NH_4HCO_3 at RT, followed by dilution to 0.8 M urea, reduction
1059 by 5 mM TCEP (37°C, 30 min) and alkylation (10 mM iodoacetamide in 100 mM NH_4HCO_3,
1060 37°C, 30 min in the dark) before overnight digestion by sequencing grade trypsin (1 µg,
1061 Promega, 37°C). After adjustment of sample pH to ~2 (using 5% TFA), peptides were de-
1062 salted on C-18 spin columns (3-30 µg capacity, The Nest group) using 0.1% TFA as acidifier
1063 in 2%/50% ACN for washing/elution. For MS measurements, peptides were dissolved in 20
1064 µl 2% ACN. 0.1% FA.

1065 ## LC-MS measurements

1066 Mass spectrometric analysis of the peptide samples generated from the chromatographic
1067 fractions was carried out on an Eksigent nanoLC Ultra 1D Plus and expert 400 autosampler
1068 system (Eksigent, Dublin, CA) coupled to a TripleTOF 6600 (Sciex, Ontario, Canada)
1069 equipped with a NanoSpray III ion source. The acquisition software was Analyst TF 1.7.1. A
1070 75 um inner diameter PicoFrit emitter (New Objective, Woburn, MA) was packed in-house
1071 with Magic C18 AQ 3 um, 200 Å particles (Bruker, Billerica, MA) to a length of 40 cm. It
1072 was operated at a flow of 300 nl/min and at room temperature. The LC solvent A was
1073 composed of 98% ultra-high quality water, 2% acetonitrile and 0.1% formic acid, LC solvent
1074 B was 98% acetonitrile, 2% ultra-high quality water and 0.1% formic acid. 3 µl of sample
1075 were loaded onto the column and separated by a linear gradient from 5 to 35% B in 60 min (or
1076 120 min for DDA and library generation purposes, see below).

1077 For the quantitative analysis of the 390 SEC fractions constituting the core sample set of the
1078 experiment, the TripleTOF was operated in SWATH mode. One MS1 survey scan was
1079 followed by 64 SWATH scans in a looped fashion. The SWATH windows are listed in
1080 Supplementary Table 1, covering precursors in the range of 400-1200 m/z with their widths
1081 chosen to obtain similar precursor intensity densities within all SWATH windows, i.e.
1082 resulting in narrower windows for m/z regions with a high density of precursors. Adjacent
1083 SWATH windows overlapped by 1 m/z to accommodate for the Q1 isolation profile. The

1084 monitored m/z range was 360-1460 in the MS1 scan and 300-2000 in the SWATH scans, the
1085 accumulation time was 200 ms and 50 ms, respectively, which resulted in a cycle time of
1086 around 3.4 s. For fragmentation, a rolling collisional energy (calculated for a theoretical 2+
1087 ion centered in the corresponding SWATH window) with a collisional energy spread of 15 eV
1088 was applied. The ion source was operated with the following settings: spray voltage, 2600 V;
1089 ion source gas flow, 16; curtain gas flow, 35; interface heater temperature, 75°C and
1090 declustering potential, 100.

1091 For the generation of a sample-specific library of peptide query parameters, 83 of the 390
1092 SEC samples, representing all replicates, elution ranges and conditions and fractions covering
1093 an extended elution range up to F89 in experimental replicate 1, were selected for analysis by
1094 data-dependent acquisition mode over prolonged LCMS gradients of 2 h per sample in order
1095 to allow for deeper coverage of the peptide query parameter library. For DDA runs, samples
1096 were separated by a 120 min linear gradient from 5 to 35% LC solvent B. One MS1 scan was
1097 followed by 20 MS2 scans with an accumulation time of 250 ms for MS1 and 100 ms for
1098 MS2. The monitored m/z range was 360-1460 for MS1 and 50-2000 for MS2. The dynamic
1099 exclusion time was set to 20 s.
1100 AP-MS samples were analyzed by LC-MS/MS on an LTQ-Orbitrap XL system (Thermo
1101 Fisher Scientific) equipped with an EASY nLC II system (Proxeon) operated in DDA mode,
1102 acquiring over an LC gradient of 5-35% of LC solvent B (98% ACN, 0.1% FA) in LC solvent
1103 A (2% ACN, 0.1% FA) in 90 min up to 10 MS/MS spectra of the up to top10 most-abundant
1104 precursors selected from intermittent MS1 survey scans (m/z range, 350-1600 m/z).
1105 Precursors analyzed were dynamically excluded from re-selection for 30 s and with an
1106 exclusion list size of maximally 300 entries. The automatic gain control (AGC) target value
1107 was set to 2e5 for full scans (MS) and 3e4 (MS/MS) scans.

1108 Data processing

1109 DDA-MS data processing

1110 For generation of the peptide query parameter library DDA-MS data acquired in 2 h gradient
1111 time from 83 SEC fractions representative of all replicates, condition and SEC elution ranges
1112 was processed by spectrum-centric analysis and then processed into a spectrum- and reduced
1113 peptide query parameter-library essentially as described(Schubert et al., 2015), except for the
1114 following adaptations: MS spectra were searched for matches to the human UniProt/SwissProt
1115 reference database (reviewed, canonical entries, build: 2017-06-19, supplemented with typical
1116 contaminant (cRAP, https://www.thegpm.org/crap/) and E. coli β-galactosidase sequences)
1117 using trypsin cleavage, 50 ppm precursor and 0.1 Da fragment ion mass tolerance,
1118 carbamidomethyl (C) as static and oxidation (M) as variable modification and allowing up to

1119 two missed cleavages. The results from four independent searches using different search
1120 engines (X!Tandem 2013.06.15.1, Ommsa 2.1.9, MyriMatch 2.1.138 and Comet 2015.02 rev.
1121 3) were integrated using iProphet of the Trans-Proteomic Pipeline ((TPP v4.7 POLAR
1122 VORTEX rev 0, Build 201403121010), filtering the results at 1% peptide FDR (0.978883
1123 iprob) as determined using the tool Mayu(Reiter et al., 2009). We intentionally chose a less
1124 strict peptide-level FDR cut-off (compared to requiring 1% FDR on protein level) in order to
1125 increase sensitivity for the recovery of true positive peptide signals which would be lost as
1126 false negatives under strict protein level FDR control but that can, in an SEC experiment, be
1127 validated by quantitative agreement with high confidence sibling peptides along SEC
1128 fractionation as assessed in downstream data filtering. The spectra were then processed into a
1129 spectral library using the tool Spectrast(Lam et al., 2010) with iRT calibration followed by the
1130 generation of a peptide query parameter library, essentially as described(Schubert et al., 2015)
1131 and within the iPortal compute infrastructure(Kunszt et al., 2015). Query parameters were
1132 composed selecting the 6 most abundant fragment ion transitions per precursor from the b or y
1133 ion series within m/z range 350-2000 and allowing fragment charge states 1-2 and no mass
1134 gains or losses. The final library contains query parameters for 111,267 precursors of 90,932
1135 peptides mapping to 9603 protein groups that were subsequently targeted for quantification in
1136 the 390 60 min gradient SWATH-MS runs of the 390 SEC fractions. Given the strict rules
1137 employed for downstream quantification (quantifying only single, unique proteins with at
1138 least 2 unique, proteotypic peptides) the number of maximally detectable analytes as
1139 constrained by the query parameter library drops to 102,629 precursors of 83,863 peptides
1140 mapping to 5,916 unique proteins. 60 min DDA-MS data were processed equivalently by
1141 spectrum-centric analysis to obtain spectral counts across chromatographic fractions as
1142 quantitative measure for technical comparisons (DDA search results and the spectral and
1143 peptide query parameter libraries are available via ProteomeXchange, see section data
1144 availability below).

1145 ### SWATH-MS data processing

1146 The SWATH -MS data were analyzed via targeted, peptide-centric analysis, querying 111,267
1147 precursors from the sample-specific peptide query parameter library (see above) in the
1148 SWATH fragment ion chromatograms, using a modified OpenSWATH(Röst et al., 2014),
1149 PyProphet (Reiter et al., 2011; Teleman et al., 2015) and TRIC(Röst et al., 2016) workflow.
1150 First, one global classifier was trained on a subsampled set of SEC fractions across the
1151 experiment using pyProphet-cli (Rosenberger et al., 2017) (Specifically, fractions 3, 43 and
1152 44 of each replicate and condition were analyzed jointly in order to generate a stable scoring
1153 function from the most analyte-rich measurements (F43 and F44) while including different
1154 analytes detected exclusively in the high MW range (F3)). Peptides from all fractions were

1155 then quantified and scored using the pre-trained scoring function using OpenSWATH,
1156 pyProphet and TRIC in the iPortal framework(Kunszt et al., 2015). TRIC was set to recover
1157 precursors at an experiment-wide assay/peptide query-level (TRIC target) FDR of 5%. The
1158 full result table (E1709051521_feature_alignment.tsv.gz) has been deposited, together with
1159 the MS raw data, to ProteomeXchange, see section data availability below.

1160 ### Downstream SEC-SWATH-MS data processing and FDR estimation

1161 Precursor-level results from E1709051521_feature_alignment.tsv were imported into
1162 *CCprofiler* extended by the protein-centric differential analysis module. Upon import,
1163 precursor intensity signals (summed intensity of the 6 most-abundant fragment ion XIC peak
1164 area) were summed per peptide (function: *importFromOpenSWATH*). Then, missing values
1165 flanked by at least two consecutive identifications were imputed by a spline fit (function:
1166 *findMissingValues*).Traces were scaled to the internal standard spike-in peptides of E. coli β-
1167 galactosidase (P00722, function: *normalizeToStandard*) followed by smoothing of total
1168 intensities according to a spline fit over total MS intensity sums (function: *smootheTraces*).
1169 The data were further filtered on chromatography-informed scores following final FDR
1170 estimation based on the simple target-decoy method. Specific filtering rules were, first,
1171 eliminating all values part of consecutive identification stretches below length three and,
1172 second, exclusion of peptides based on their quantitative fractionation pattern's average
1173 dissimilarity to those of sibling peptides (originating from the same parent protein). Guided
1174 by the fraction of decoys remaining (target: 3% on unique protein identifier level), peptides
1175 with average sibling peptide correlation coefficient (spc) below [0.28 - 0.34] were removed,
1176 with cut-offs selected to achieve a decoy rate below 3% among the remaining protein entries.
1177 Subsequently, proteins were quantified by summing the top2 most-intense peptide signals.
1178 Protein intensity across the replicates was averaged and standard errors of the mean
1179 calculated. Cumulatively, 5044 proteins were characterized. The FDR on protein level was
1180 estimated based on the simple target-decoy method, with correction for the fraction of false
1181 protein targets (equivalent to the fraction of absent proteins, π_A(The et al., 2016)). We
1182 estimate π_A as the fraction of library-contained target proteins that were not detected with
1183 high confidence in the targeted analysis, i.e. $\pi_A \approx (5{,}916 - 5{,}044) / 5{,}916 = 0.147$. This
1184 estimation is conservative because not all true positive proteins are recovered at high
1185 confidence, leading to overestimation of π_A and thus more conservative corrected FDR
1186 estimates. Accordingly, 135 decoy entries passing the filters together with the 5044 target
1187 proteins (decoy rate, 0.026) point to an estimated global protein level FDR of (135 * 0.147) /
1188 5,044 = 0.0039, ≤ 0.4%.

1189 ### Protein-centric differential SEC distribution testing

1190 To detect proteins that significantly alter their quantitative SEC elution pattern we devised a
1191 protein-centric differential analysis pipeline that leverages all information on peptide level to
1192 identify proteins that shift elution behavior across distinct SEC ranges of elution (elution
1193 features). First, the global set of protein elution features apparent from the dataset were
1194 detected from an integrated set of peptide chromatograms (traces) using the SECprofiler
1195 framework, followed by statistical testing for differences based on the intensities observed in
1196 the different experimental replicates. Specifically, peptide traces were averaged within the
1197 conditions and then artificially combined into one summed set of 60891 traces (function
1198 *integrateTraceIntensities*). Then, high confidence protein elution features were detected as
1199 signals of co-peaking peptide traces, grouping the traces by parent protein identifier and
1200 including decoys with randomized peptide-to-protein mapping (functions:
1201 *findProteinFeatures*, *calculateCoelutionScore* and *calculateQvalue*). At a q-value cut-off of
1202 5%, 6044 protein elution features were detected to define the ranges for differential
1203 abundance tests.

1204 To detect differential SEC elution behavior, peptide abundances in the elution ranges were
1205 then tested for significant differences in abundance, using the functions *extractFeatureVals*
1206 and *testDifferentialExpression* and employing the paired t-test as statistical metric. All tests
1207 were based on the raw variability of the data, i.e. minimally processed data points (essentially,
1208 only scaled within conditions), to avoid biases introduced by data processing. Missing values
1209 were replaced by uniformly sampled intensities in the 5th percentile of quantified values. The
1210 test results were collected on protein level by deriving a fold-change adjusted median p-value
1211 from all peptide tests mapping to the respective parent proteins (Suomi and Elo, 2017). Using
1212 the function *aggregatePeptideTests* the protein level significance was calculated using a
1213 cumulative beta distribution parametrized on the number observed of peptides (Suomi and
1214 Elo, 2017). This resulted in protein p-values for 1-5 individual features per protein with
1215 separate scoring. To simplify visualization and reduce the results to one set of scores per
1216 protein, for each protein the lowest pBHadj and largest fold-change of which was selected for
1217 visualization in the screen hit volcano plot (See **Figure 1 D**). The R package *CCprofiler*,
1218 extended by the protein-centric differential analysis module is available via GitHub
1219 (https://github.com/CCprofiler/CCprofiler/tree/helaCC).

1220 ### AP-MS data analysis

1221 AP-MS DDA-MS data were analyzed by spectrum-centric analysis matching spectra against
1222 the human reviewed SwissProt reference sequence database (build 2018-08-01) using three
1223 search engines (X!Tandem, Myrimatch and Comet) and result integration via the Trans-

1224 proteomic pipeline (TPP), applying FDR cut-offs of 1% at the peptide level (iprophet-
1225 pepFDR, ≥ 0.6581 iprobability) and protein level (ProteinProphet), executed within the iportal
1226 framework (Kunszt et al., 2015). Searches allowed mass tolerances of 15 ppm and 0.4 Da on
1227 precursor and fragment ion level. Enzyme specificity was set to Trypsin, allowing up to two
1228 missed cleavages. Carbamidomethyl was set as static modification, no variable modifications
1229 were considered.

1230 Assignment of Nuclear pore complex components

1231 Nuclear pore complex members were assigned based on two consecutively applied criteria, i)
1232 Uniprot query (nuclear pore complex AND reviewed:yes AND organism:"Homo sapiens
1233 (Human) [9606]") and ii) structural assignment in Table 1 by Hoelz et al. (Hoelz et al., 2016),
1234 resulting in 32 canonical subunits employed for benchmarking and exploration of NPC
1235 disassembly sub-complexes.

1236 Statistical protein set enrichment and testing of over represented protein sets

1237 Statistical over representation of protein functional groups among the protein sets of interest
1238 was performed in the PANTHER classification system (http://pantherdb.org/, Release 14.1)
1239 using the Statistical over representation test (Fisher's exact test), testing against the
1240 background of all detected proteins (n = 6,010, **Figure 3**, **Figure 4** and **Supplemental Figure**
1241 **S3A**) or the full human genome background (**Supplemental Figure S3C**).

1242 Data availability

1243 The mass spectrometry proteomics raw data and processing results have been deposited to the
1244 ProteomeXchange Consortium (http://proteomecentral.proteomexchange.org) via the PRIDE
1245 partner repository(Vizcaíno et al., 2012) with the dataset identifier PXD010288. The data are
1246 available in easily browsable and searchable form via https://sec-
1247 explorer.shinyapps.io/hela_cellcycle/ where the full dataset can be accessed using the
1248 password "ethsecexplorer".

1249 Supplemental Information

1250 The supplemental information entails six Supplemental Figures (S1-S6), one Supplemental
1251 Item (SI1) and three Supplemental Tables (ST1-3) with self-contained legends where
1252 applicable and the following titles.

1253 Supplemental Figure S1: Validation of homogenous cell cycle arrest and of inducible Nup58-
1254 expressing HeLa cell lines

1255 Supplemental Figure S2: Benchmarking the SEC-SWATH-MS workflow - correction of
1256 longitudinal effects and replicate intensity correlation

1257 Supplemental Figure S3: Pathway enrichment among top 1000 proteins recovered by size or
1258 thermostability profiling along the cell cycle

1259 Supplemental Figure S4: Protein elution peak detection and properties of multi-complex
1260 signal proteins

1261 Supplemental Figure S5: Investigation of RAP1-TRF2-IKK cross-complex interaction and
1262 zoom-in to NUP93 subpopulations resolved across mitotic states

1263 Supplemental Figure S6: Investigation of SEC13 moonlighting across Nup107-160
1264 subcomplex and COPII vesicle transport related complexes.

1265 Supplemental Item SI1: SEC-SWATH-MS protein chromatogram plots

1266 Supplemental Table ST1: Global protein quantification summary table

1267 Supplemental Table ST2: Global protein elution peak detection and statistical scoring
1268 summary table

1269 Supplemental Table ST3: Global complex remodeling summary table

1270 References

1271 Aebersold, R., and Mann, M. (2016). Mass-spectrometric exploration of proteome structure
1272 and function. Nature *537*, 347–355.

1273 Arat, N.Ö., and Griffith, J.D. (2012). Human Rap1 Interacts Directly with Telomeric DNA
1274 and Regulates TRF2 Localization at the Telomere. J. Biol. Chem. *287*, 41583–41594.

1275 Bache, N., Geyer, P.E., Bekker-Jensen, D.B., Hoerning, O., Falkenby, L., Treit, P. V, Doll, S.,
1276 Paron, I., Müller, J.B., Meier, F., et al. (2018). A Novel LC System Embeds Analytes in Pre-
1277 formed Gradients for Rapid, Ultra-robust Proteomics. Mol. Cell. Proteomics *17*, 2284–2296.

1278 Becher, I., Andrés-Pons, A., Romanov, N., Stein, F., Schramm, M., Baudin, F., Helm, D.,
1279 Kurzawa, N., Mateus, A., Mackmull, M.T., et al. (2018). Pervasive Protein Thermal Stability
1280 Variation during the Cell Cycle. Cell *173*, 1495-1507.e18.

1281 Beck, M., and Hurt, E. (2017). The nuclear pore complex: understanding its function through
1282 structural insight. Nat. Rev. Mol. Cell Biol. *18*, 73–89.

1283 Chug, H., Trakhanov, S., Hülsmann, B.B., Pleiner, T., and Görlich, D. (2015). Crystal
1284 structure of the metazoan Nup62•Nup58•Nup54 nucleoporin complex. Science (80-.). *350*,
1285 106–110.

1286 Collins, B.C., Gillet, L.C., Rosenberger, G., Röst, H.L., Vichalkovski, A., Gstaiger, M., and
1287 Aebersold, R. (2013). Quantifying protein interaction dynamics by SWATH mass
1288 spectrometry: application to the 14-3-3 system. Nat. Methods *10*, 1246–1253.

1289 Collins, B.C., Hunter, C.L., Liu, Y., Schilling, B., Rosenberger, G., Bader, S.L., Chan, D.W.,
1290 Gibson, B.W., Gingras, A.-C., Held, J.M., et al. (2017). Multi-laboratory assessment of
1291 reproducibility, qualitative and quantitative performance of SWATH-mass spectrometry. Nat.
1292 Commun. *8*, 291.

1293 Dai, L., Zhao, T., Bisteau, X., Sun, W., Prabhu, N., Lim, Y.T., Sobota, R.M., Kaldis, P., and
1294 Nordlund, P. (2018). Modulation of Protein-Interaction States through the Cell Cycle. Cell
1295 *173*, 1481-1494.e13.

1296 Dominguez, D., Tsai, Y.-H., Weatheritt, R., Wang, Y., Blencowe, B.J., Wang, Z., Matese, J.,
1297 Perou, C., Hurt, M., Brown, P., et al. (2016). An extensive program of periodic alternative
1298 splicing linked to cell cycle progression. Elife *5*, 191–207.

1299 Dong, M., Yang, L.L., Williams, K., Fisher, S.J., Hall, S.C., Biggin, M.D., Jin, J., and
1300 Witkowska, H.E. (2008). A "tagless" strategy for identification of stable protein complexes
1301 genome-wide by multidimensional orthogonal chromatographic separation and iTRAQ
1302 reagent tracking. J. Proteome Res. *7*, 1836–1849.

1303 Dunkley, T.P.J., Watson, R., Griffin, J.L., Dupree, P., and Lilley, K.S. (2004). Localization of
1304 organelle proteins by isotope tagging (LOPIT). Mol. Cell. Proteomics *3*, 1128–1134.

1305 Foster, L.J., de Hoog, C.L., Zhang, Y., Zhang, Y., Xie, X., Mootha, V.K., and Mann, M.
1306 (2006). A mammalian organelle map by protein correlation profiling. Cell *125*, 187–199.

1307 Gavet, O., and Pines, J. (2010). Activation of cyclin B1–Cdk1 synchronizes events in the
1308 nucleus and the cytoplasm at mitosis. J. Cell Biol. *189*, 247–259.

1309 Gillet, L.C., Navarro, P., Tate, S., Röst, H., Selevsek, N., Reiter, L., Bonner, R., and
1310 Aebersold, R. (2012). Targeted data extraction of the MS/MS spectra generated by data-
1311 independent acquisition: a new concept for consistent and accurate proteome analysis. Mol.
1312 Cell. Proteomics *11*, O111.016717.

1313 Gillet, L.C., Leitner, A., and Aebersold, R. (2016). Mass Spectrometry Applied to Bottom-Up
1314 Proteomics: Entering the High-Throughput Era for Hypothesis Testing. Annu. Rev. Anal.
1315 Chem. *9*, 449–472.

1316 Gong, D., Pomerening, J.R., Myers, J.W., Gustavsson, C., Jones, J.T., Hahn, A.T., Meyer, T.,
1317 and Ferrell Jr., J.E. (2007). Cyclin A2 Regulates Nuclear-Envelope Breakdown and the
1318 Nuclear Accumulation of Cyclin B1. Curr. Biol. *17*, 85–91.

1319 Häfner, J., Mayr, M.I., Möckel, M.M., and Mayer, T.U. (2014). Pre-anaphase chromosome
1320 oscillations are regulated by the antagonistic activities of Cdk1 and PP1 on Kif18A. Nat.
1321 Commun. *5*, 4397.

1322 Hartwell, L.H., Hopfield, J.J., Leibler, S., and Murray, A.W. (1999). From molecular to
1323 modular cell biology. Nature *402*, C47-52.

1324 Heusel, M., Bludau, I., Rosenberger, G., Hafen, R., Frank, M., Banaei-Esfahani, A., Drogen,
1325 A. van, Collins, B.C., Gstaiger, M., and Aebersold, R. (2019). Complex-centric proteome
1326 profiling by SEC-SWATH-MS. Mol. Syst. Biol. *15*, e8438.

1327 Hoelz, A., Glavy, J.S., and Beck, M. (2016). Toward the atomic structure of the nuclear pore
1328 complex: when top down meets bottom up. Nat. Struct. Mol. Biol. *23*, 624–630.

1329 Ideker, T., Galitski, T., and Hood, L. (2001). A new approach to decoding life: systems
1330 biology. Annu. Rev. Genomics Hum. Genet. *2*, 343–372.

1331 Itzhak, D.N., Tyanova, S., Cox, J., and Borner, G.H. (2016). Global, quantitative and dynamic
1332 mapping of protein subcellular localization. Elife *5*.

1333 Kristensen, A.R., Gsponer, J., and Foster, L.J. (2012). A high-throughput approach for
1334 measuring temporal changes in the interactome. Nat. Methods *9*, 907–909.

1335 Kunszt, P., Blum, L., Hullár, B., Schmid, E., Srebniak, A., Wolski, W., Rinn, B., Elmer, F.-J.,
1336 Ramakrishnan, C., Quandt, A., et al. (2015). iPortal: the swiss grid proteomics portal:
1337 Requirements and new features based on experience and usability considerations. Concurr.
1338 Comput. Pract. Exp. *27*, 433–445.

1339 Lam, H., Deutsch, E.W., and Aebersold, R. (2010). Artificial decoy spectral libraries for false
1340 discovery rate estimation in spectral library searching in proteomics. J. Proteome Res. *9*, 605–
1341 610.

1342 Larance, M., Kirkwood, K.J., Tinti, M., Brenes Murillo, A., Ferguson, M.A.J., and Lamond,
1343 A.I. (2016). Global Membrane Protein Interactome Analysis using *In vivo* Crosslinking and
1344 Mass Spectrometry-based Protein Correlation Profiling. Mol. Cell. Proteomics *15*, 2476–
1345 2490.

1346 Laurell, E., Beck, K., Krupina, K., Theerthagiri, G., Bodenmiller, B., Horvath, P., Aebersold,
1347 R., Antonin, W., and Kutay, U. (2011). Phosphorylation of Nup98 by Multiple Kinases Is
1348 Crucial for NPC Disassembly during Mitotic Entry. Cell *144*, 539–550.

1349 Leuenberger, P., Ganscha, S., Kahraman, A., Cappelletti, V., Boersema, P.J., von Mering, C.,
1350 Claassen, M., and Picotti, P. (2017). Cell-wide analysis of protein thermal unfolding reveals
1351 determinants of thermostability. Science (80-.). *355*, eaai7825.

1352 Lin, D.H., Stuwe, T., Schilbach, S., Rundlet, E.J., Perriches, T., Mobbs, G., Fan, Y.,
1353 Thierbach, K., Huber, F.M., Collins, L.N., et al. (2016). Architecture of the symmetric core of
1354 the nuclear pore. Science (80-.). *352*, aaf1015–aaf1015.

1355 Linder, M.I., Köhler, M., Boersema, P., Weberruss, M., Wandke, C., Marino, J., Ashiono, C.,
1356 Picotti, P., Antonin, W., and Kutay, U. (2017). Mitotic Disassembly of Nuclear Pore
1357 Complexes Involves CDK1- and PLK1-Mediated Phosphorylation of Key Interconnecting
1358 Nucleoporins. Dev. Cell *43*, 141-156.e7.

1359 Liu, F., and Fitzgerald, M.C. (2016). Large-Scale Analysis of Breast Cancer-Related
1360 Conformational Changes in Proteins Using Limited Proteolysis. J. Proteome Res. *15*, 4666–
1361 4674.

1362 Liu, D., Safari, A., O'Connor, M.S., Chan, D.W., Laegeler, A., Qin, J., and Songyang, Z.
1363 (2004). PTOP interacts with POT1 and regulates its localization to telomeres. Nat. Cell Biol.
1364 *6*, 673–680.

1365 Liu, X., Yang, W., Gao, Q., and Regnier, F. (2008). Toward chromatographic analysis of
1366 interacting protein networks. J. Chromatogr. A *1178*, 24–32.

1367 Ludwig, C., and Aebersold, R. Getting Absolute : Determining Absolute Protein Quantities
1368 via Selected Reaction Monitoring Mass Spectrometry. 80–109.

1369 Ly, T., Endo, A., and Lamond, A.I. (2015). Proteomic analysis of the response to cell cycle
1370 arrests in human myeloid leukemia cells. Elife *4*.

1371 Nigg, E.A. (1993). Cellular substrates of p34(cdc2) and its companion cyclin-dependent
1372 kinases. Trends Cell Biol. *3*, 296–301.

1373 Peyressatre, M., Prével, C., Pellerano, M., and Morris, M.C. (2015). Targeting cyclin-
1374 dependent kinases in human cancers: from small molecules to Peptide inhibitors. Cancers
1375 (Basel). *7*, 179–237.

1376 Reiter, L., Claassen, M., Schrimpf, S.P., Jovanovic, M., Schmidt, A., Buhmann, J.M.,
1377 Hengartner, M.O., and Aebersold, R. (2009). Protein identification false discovery rates for

very large proteomics data sets generated by tandem mass spectrometry. Mol. Cell. Proteomics *8*, 2405–2417.

Reiter, L., Rinner, O., Picotti, P., Hüttenhain, R., Beck, M., Brusniak, M.-Y., Hengartner, M.O., and Aebersold, R. (2011). mProphet: automated data processing and statistical validation for large-scale SRM experiments. Nat. Methods *8*, 430–435.

Rosenberger, G., Ludwig, C., Röst, H.L., Aebersold, R., and Malmström, L. (2014). aLFQ: an R-package for estimating absolute protein quantities from label-free LC-MS/MS proteomics data. Bioinformatics *30*, 2511–2513.

Rosenberger, G., Bludau, I., Schmitt, U., Heusel, M., Hunter, C.L., Liu, Y., MacCoss, M.J., MacLean, B.X., Nesvizhskii, A.I., Pedrioli, P.G.A., et al. (2017). Statistical control of peptide and protein error rates in large-scale targeted data-independent acquisition analyses. Nat. Methods *14*, 921–927.

Röst, H.L., Rosenberger, G., Navarro, P., Gillet, L., Miladinović, S.M., Schubert, O.T., Wolski, W., Collins, B.C., Malmström, J., Malmström, L., et al. (2014). OpenSWATH enables automated, targeted analysis of data-independent acquisition MS data. Nat. Biotechnol. *32*, 219–223.

Röst, H.L., Liu, Y., D'Agostino, G., Zanella, M., Navarro, P., Rosenberger, G., Collins, B.C., Gillet, L., Testa, G., Malmström, L., et al. (2016). TRIC: an automated alignment strategy for reproducible protein quantification in targeted proteomics. Nat. Methods *13*, 777–783.

Ruepp, A., Waegele, B., Lechner, M., Brauner, B., Dunger-Kaltenbach, I., Fobo, G., Frishman, G., Montrone, C., and Mewes, H.-W. (2010). CORUM: the comprehensive resource of mammalian protein complexes--2009. Nucleic Acids Res. *38*, D497-501.

Schopper, S., Kahraman, A., Leuenberger, P., Feng, Y., Piazza, I., Müller, O., Boersema, P.J., and Picotti, P. (2017). Measuring protein structural changes on a proteome-wide scale using limited proteolysis-coupled mass spectrometry. Nat. Protoc. *12*, 2391–2410.

Schubert, O.T., Gillet, L.C., Collins, B.C., Navarro, P., Rosenberger, G., Wolski, W.E., Lam, H., Amodei, D., Mallick, P., MacLean, B., et al. (2015). Building high-quality assay libraries for targeted analysis of SWATH MS data. Nat. Protoc. *10*, 426–441.

Scott, N.E., Rogers, L.D., Prudova, A., Brown, N.F., Fortelny, N., Overall, C.M., and Foster, L.J. (2017). Interactome disassembly during apoptosis occurs independent of caspase cleavage. Mol. Syst. Biol. *13*, 906.

Stacey, R.G., Skinnider, M.A., Scott, N.E., and Foster, L.J. (2017). A rapid and accurate approach for prediction of interactomes from co-elution data (PrInCE). BioRxiv 152355.

Suomi, T., and Elo, L.L. (2017). Enhanced differential expression statistics for data-independent acquisition proteomics. Sci. Rep. *7*, 5869.

Szklarczyk, D., Morris, J.H., Cook, H., Kuhn, M., Wyder, S., Simonovic, M., Santos, A., Doncheva, N.T., Roth, A., Bork, P., et al. (2017). The STRING database in 2017: quality-controlled protein–protein association networks, made broadly accessible. Nucleic Acids Res. *45*, D362–D368.

Tan, C.S.H., Go, K.D., Bisteau, X., Dai, L., Yong, C.H., Prabhu, N., Ozturk, M.B., Lim, Y.T., Sreekumar, L., Lengqvist, J., et al. (2018). Thermal proximity coaggregation for system-wide profiling of protein complex dynamics in cells. Science *359*, 1170–1177.

Tang, B.L., Peter, F., Krijnse-Locker, J., Low, S.H., Griffiths, G., and Hong, W. (1997). The

1421 mammalian homolog of yeast Sec13p is enriched in the intermediate compartment and is
1422 essential for protein transport from the endoplasmic reticulum to the Golgi apparatus. Mol.
1423 Cell. Biol. *17*, 256–266.

1424 Teleman, J., Röst, H.L., Rosenberger, G., Schmitt, U., Malmström, L., Malmström, J., and
1425 Levander, F. (2015). DIANA--algorithmic improvements for analysis of data-independent
1426 acquisition MS data. Bioinformatics *31*, 555–562.

1427 Teo, H., Ghosh, S., Luesch, H., Ghosh, A., Wong, E.T., Malik, N., Orth, A., de Jesus, P.,
1428 Perry, A.S., Oliver, J.D., et al. (2010). Telomere-independent Rap1 is an IKK adaptor and
1429 regulates NF-κB-dependent gene expression. Nat. Cell Biol. *12*, 758–767.

1430 The, M., Tasnim, A., and Käll, L. (2016). How to talk about protein-level false discovery
1431 rates in shotgun proteomics. Proteomics *16*, 2461–2469.

1432 Vermeulen, K., Van Bockstaele, D.R., and Berneman, Z.N. (2003). The cell cycle: a review of
1433 regulation, deregulation and therapeutic targets in cancer. Cell Prolif. *36*, 131–149.

1434 Vizcaíno, J.A., Côté, R.G., Csordas, A., Dianes, J.A., Fabregat, A., Foster, J.M., Griss, J.,
1435 Alpi, E., Birim, M., Contell, J., et al. (2012). The Proteomics Identifications (PRIDE)
1436 database and associated tools: status in 2013. Nucleic Acids Res. *41*, D1063–D1069.

1437 Wan, C., Borgeson, B., Phanse, S., Tu, F., Drew, K., Clark, G., Xiong, X., Kagan, O., Kwan,
1438 J., Bezginov, A., et al. (2015). Panorama of ancient metazoan macromolecular complexes.
1439 Nature.

1440 Wessels, H.J.C.T., Vogel, R.O., van den Heuvel, L., Smeitink, J.A., Rodenburg, R.J.,
1441 Nijtmans, L.G., and Farhoud, M.H. (2009). LC-MS/MS as an alternative for SDS-PAGE in
1442 blue native analysis of protein complexes. Proteomics *9*, 4221–4228.

1443 Xu, Y., Strickland, E.C., and Fitzgerald, M.C. (2014). Thermodynamic Analysis of Protein
1444 Folding and Stability Using a Tryptophan Modification Protocol. Anal. Chem. *86*, 7041–
1445 7048.

1446 Yoshikawa, H., Larance, M., Harney, D.J., Sundaramoorthy, R., Ly, T., Owen-Hughes, T.,
1447 and Lamond, A.I. (2018). Efficient analysis of mammalian polysomes in cells and tissues
1448 using Ribo Mega-SEC. Elife *7*.

1449 Zemp, I., Wild, T., O'Donohue, M.-F., Wandrey, F., Widmann, B., Gleizes, P.-E., and Kutay,
1450 U. (2009). Distinct cytoplasmic maturation steps of 40S ribosomal subunit precursors require
1451 hRio2. J. Cell Biol. *185*, 1167–1180.